A Fiber-coupled Optical Delivery System for a 2D$^+$ Magneto-optical Trap

by

Samuel Moir

A THESIS SUBMITTED IN PARTIAL FULFILLMENT OF THE REQUIREMENTS FOR THE DEGREE OF

Bachelor of Science

Supervisor(s):	B. Barrett, Assistant Professor, Dept. of Physics
Examining Board:	J. Thayyil, Professor, Dept. of Physics, Chair
	B. Balcom, Professor, Dept. of Physics

THE UNIVERSITY OF NEW BRUNSWICK

May, 2023

Abstract

Laser cooling of atoms can be used to produce high-sensitivity measurements of atomic phenomena. Precision optics are required to generate high-quality measurements. This study characterizes the properties of a fiber-coupled optical system used in the University of New Brunswick's Quantum Sensing and Ultracold Matter lab. It finds that an acousto-optic modulator transfers 79.1% of light into the first-order beam; that a mechanical shutter blocks out incident light $\sim 1\,\mathrm{ms}$ after it begins closing; and that the optical path has relative stability 5×10^{-4} over a 2 h stable period or relative stability 2×10^{-2} over a 15 h period.

Acknowledgements

Dr. Brynle Barrett provided incalculable support in explaining the process of laser cooling and the concepts behind testing and characterizing data, along with a great deal of guidance and leadership through conducting research and writing this thesis. The other researchers in the Quantum Sensing and Ultracold Matter lab (Kamal Shalaby, Tim Hunt, and Dante Batillana) provided support through my work in the lab. I found Dr. Dennis Tokaryk's knowledge of optics and optical power measurement invaluable. Brian Titus and Dr. Torsten Reuschel provided critical aid in designing and constructing circuits and measurement devices used in my study.

Table of Contents

List of Tables

List of Figures

List of Symbols, Nomenclature or Abbreviations

AOM	Acousto-optic modulator
APP	Anamorphic prism pair
DAC	Data acquisition card
LC	Left-hand circular
MOT	Magneto-optical trap
NA	Numerical aperture
PBS	Polarizing beamsplitter
PCB	Printed circuit board
PM	Polarization-maintaining
PZT	Piezoelectric transducer
QSUM	Quantum Sensing and Ultracold Matter
RHC	Right-hand circular
TTL	Transistor-transistor logic

Chapter 1

Introduction

Laser cooling is now a well-established field of atomic physics that allows for precision measurements of a range of fundamental constants and has been instrumental in winning two Nobel prizes in the past twenty years (see [1], [2]). Dr. Brynle Barrett recently established the Quantum Sensing and Ultracold Matter (QSUM) lab at UNB that will apply the laser cooling technique for a variety of experiments. To achieve this goal, this thesis focuses on the design, construction, and characterization of a fiber-splitting pathway and optical delivery system for a $2D^+$ magneto-optical trap (MOT). This will be the first stage of a 3-stage laser cooling experiment to reach nano-Kelvin temperatures.

A $2D^+$-MOT consists of a 2D-MOT and a push-beam that generates a flow of cold atoms from a source to the experimental 3D-MOT chamber. The 2D-MOT consists of two trapping lasers that cool atoms and hold them in place across the long axis of the trap. The push-beam laser (indicated by the "+" in $2D^+$-MOT) acts along the long axis of the trap to push atoms into the trapping region. These are discussed in more detail in Chapter 2.

This honours thesis is organized in three overarching sections: in the first, the theory behind laser cooling and trapping of atoms is discussed. This is followed by a

discussion of the optical components used in the splitting pathway. Finally, results of the characterization of the path are presented with analysis.

Chapter 2 begins with an overview of the principles of laser cooling. A discussion of cooling for a simplified two-level atom is presented, followed by a brief discussion of the cooling of Rubidium. Next, the principles of magneto-optical trapping are laid out. They are applied in particular to the two-dimensional case.

Chapter 3 discusses the optical pathway and delivery system necessary for the $2D^+$-MOT. This involves descriptions of the methods used to split the beam, turn it on and off quickly, and shape the spatial beam profile. Fiber-optic cables are also introduced in this chapter.

Chapter 4 presents results from measures of the speed with which the optical system can be turned on and off and the fiber-optic coupling efficiency and stability. Analysis involves measures of correlation between parameters and identifying possible causes for outliers in datasets.

Finally, Chapter 5 presents a conclusion with directions for future work.

Chapter 2

Laser Cooling and the 2D$^+$-MOT

This chapter discusses the principles of laser cooling and trapping of neutral atoms, and the specific case of the 2D$^+$-MOT.

2.1 Principles of Laser Cooling

Laser cooling of neutral atoms was first demonstrated in the landmark work by Wineland, Drullinger and Walls [3]. They applied a method of laser cooling known as "Doppler cooling" that uses radiation pressure to cool neutral Mg atoms to below 40 K. This method differentially accelerates atoms based on their direction of motion by selective excitation using the Doppler effect. Since this first implementation, methods have been greatly refined so that sub-µK temperatures are achievable [4]. The Quantum Sensing and Ultracold Matter (QSUM) lab at UNB intends to trap and cool neutral ^{87}Rb atoms. This is the most common species used in laser cooling experiments largely for historical reasons, but also due to the availability of high-powered lasers at 780 nm (the D2 transition wavelength of rubidium-87) along with its low melting point/high vapour pressure (see, for instance, [5]).

There are a variety of reasons to apply methods of laser cooling. These range from gravimetry [6] to studies of Bose-Einstein Condensates (BECs) [7]. The QSUM

lab plans to apply laser cooling to realize a quantum gravimeter based on cold-atom interferometry.

In this section, the principles of laser cooling are discussed. First, a model of a two-level atom is presented, followed by a description of the process of Doppler cooling. A full discussion of how this scales to 3D and multi-level atoms is beyond the scope of this thesis, though a short discussion of the methods for cooling ^{87}Rb is provided.

2.1.1 Model of a Two-level Atom

Consider a two-level atom (see Fig. 2.1) with ground state $|g\rangle$ and excited state $|e\rangle$. These states are separated by some energy ε_0, and can be excited by an electromagnetic wave with corresponding energy $\varepsilon_0 = \hbar\omega_0$. The frequency ω_0 is often referred to as the "resonance frequency" of the atom.

Consider a laser modelled by an electromagnetic wave propagating along the $\hat{z}$-direction, $\vec{\mathcal{E}} = \vec{E}_0 \cos(kz - \omega_L t)$, where ω_L is the frequency of the laser. $\vec{E}_0$ is the electric field amplitude, which is proportional to the square root of the laser intensity $|\vec{E}_0| \propto \sqrt{I}$. It is possible to define the Rabi frequency in this field as

$$\Omega = \frac{-q\vec{E}_0}{\hbar} \cdot \langle e| \vec{r} |g\rangle \tag{2.1}$$

which is proportional to the energy associated with the electric dipole interaction: $\langle e| q\vec{r} |g\rangle \cdot \vec{E}_0$. The Rabi frequency can be interpreted as the frequency at which the probability amplitude of the upper state oscillates in the applied electric field. Specifically, when the laser frequency ω_L is set to the resonance frequency ω_0, the probability of the atom being in either state oscillates in time at the Rabi frequency. This describes the dynamics of stimulated absorption (emission) of photons into (from) the laser field. The atom can also emit a photon (in a transition from the

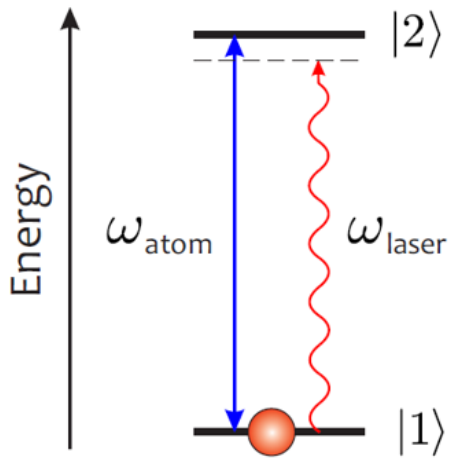

Figure 2.1: Model of a two-level atom with resonance ω_{atom} in an electric field varying with frequency ω_{laser}. States $|1\rangle$ and $|2\rangle$ correspond to the ground $|g\rangle$ and excited $|e\rangle$ states, respectively.

excited state to the ground state) spontaneously in a random direction.

Take an atom in its excited state. The process of spontaneous emission implies that the atom will likely drop back to the ground state given enough time. The rate of spontaneous emission is here referred to as Γ.

Suppose ω_L, the frequency of the laser incident on the two-level atom described above, is detuned from resonance by an amount $\delta = \omega_L - \omega_0$. Examination of the density matrix of the two-level atom in the presence of the laser field (performed elsewhere, see i.e. [4]) reveals the probability that the atom be found in the excited state follows the relationship

$$\rho_{ee} = \frac{s_0/2}{1 + s_0 + (\delta/\Gamma)^2} \tag{2.2}$$

where s_0, known as the on-resonance saturation parameter, is defined by $s_0 \equiv |\Omega|^2/\Gamma^2 = I/I_s$ (where I_s is the saturation intensity if the transition). This parameter describes the saturation of the excited state population as the intensity of the laser increases (for $I \gg I_s \rightarrow s_0 \gg 1 \implies \rho_{ee} \rightarrow \frac{1}{2}$). Eq. 2.2 is the steady-state population of the excited state, which has a characteristic resonant behaviour

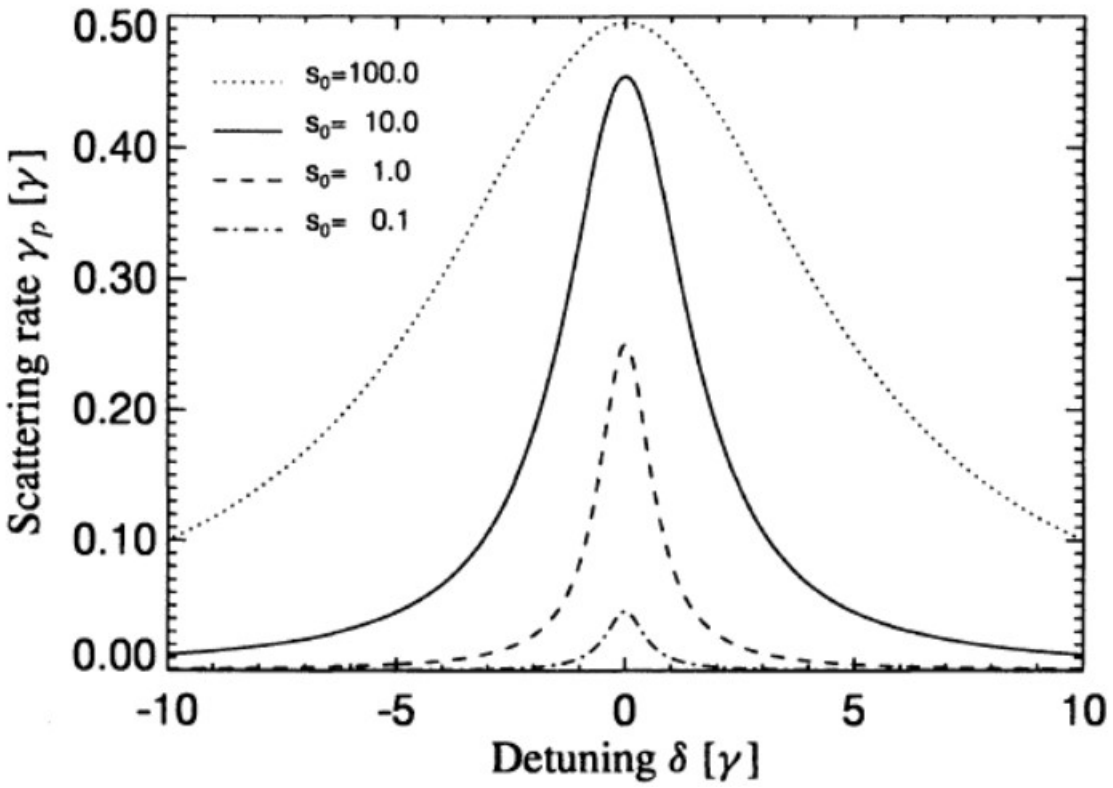

Figure 2.2: Scattering rate vs. excitation frequency detuning. The different curves show the same relationship for different saturation parameters s_0.

(Lorentzian profile) as a function of δ.

The quantity ρ_{ee} is important because it makes it possible to determine how many photons are scattered (on average, per atom) at different laser frequencies. Scattered here means absorbed and re-emitted in a new random direction. This "scattering rate" $\gamma_p = \Gamma\rho_{ee}$ also determines the radiation pressure force responsible for cooling, as will be shown. It is possible to plot the scattering rate of photons γ_p for different detunings as a measure of ρ_{ee} (see Fig. 2.2).

2.1.2 Doppler Cooling of an Atom in One Dimension

Consider a two-level atom of resonance frequency ω_0 moving in one dimension along a beam of coherent light of frequency ω_L. The light has an electric field $\vec{\mathcal{E}} = E_0 \cos(kz - \omega_L t)\hat{\varepsilon}$. The atom sees a relativistic Doppler shift in the frequency of light it observes

governed by

$$\omega(v, \omega_L) = \omega_L \sqrt{\frac{1 + v/c}{1 - v/c}}. \tag{2.3}$$

If $v \ll c$ (as intended in the case of cooling atoms) this simplifies to

$$\omega(v, \omega_L) \approx \omega_L(1 + \tfrac{v}{c}) = \omega_L + k_L v \tag{2.4}$$

where $k_L = \omega_L/c$ is the Doppler shift coefficient and $\vec{v}$ is the signed 1D speed of the light source in the atom's frame (or, equivalently, the velocity of the atom in the lab frame). In the above formulation, $v > 0$ if the atom is moving toward the source.

Because of this Doppler shift, the atom will observe different frequencies of light ω for the same ω_L depending on its speed and direction of motion. Thus, ω_L can be set so that $\omega(v, \omega_L) = \omega_0$ for a particular velocity, not others.

Suppose ω_L is set such that $\omega = \omega_0$ for a particular velocity $\vec{v} > 0$. When an atom of $\vec{v}$ excites, it absorbs an incident photon (see Fig 2.3). By conservation of momentum, the atom's speed must be reduced by $\vec{v}^* = \vec{v} - \hbar\vec{k}_L/M$ where M is the mass of the atom being excited. Eventually, the atom decays back to its ground state. In doing so, it re-emits a photon with some momentum $\hbar\vec{k}_2$ as in the third time-step in Fig. 2.3. In the simplified 1D case, this photon can either be re-emitted in the direction of the light source or against the direction of the light source. In the first case, $\vec{v}_{f,1} = \vec{v}_i - 2\hbar(\vec{k}_1 - \vec{k}_2)/M$ and the speed of the atom is further reduced. In the second, $\vec{v}_{f,2} = \vec{v}_i$ since the re-emitted photon has the same momentum as the original. Either case is equally likely, so on average, the final speed of an atom after the excitation-decay process is $\langle\vec{v}\rangle = (\vec{v}_{f,1} + \vec{v}_{f,2})/2 = \vec{v}_i - \hbar\vec{k}_1/M$. Thus the speed of a particular atom originally in the v class is, on average, reduced.

This can be extended to 3D, as shown in Fig. 2.3, where now the absorbed photon $\hbar\vec{k}_1$ has direction of motion along the laser's propagation direction, and the spontaneously-emitted photon $\hbar\vec{k}_2$ occurs in a random direction with equal proba-

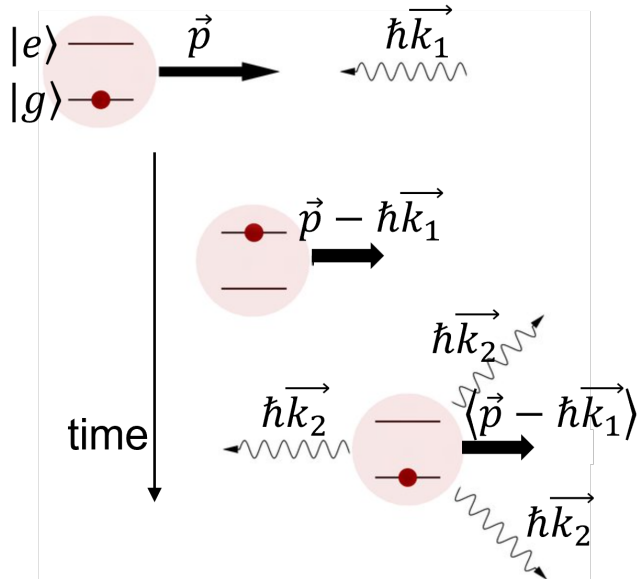

Figure 2.3: An atom with velocity $\vec{v}$ (momentum $\vec{p}$) absorbs a photon. It enters its excited state and its momentum is reduced before decaying by releasing a photon in a random direction.

bility. Averaging over the surface of a sphere about the atom, the same result is obtained: $\langle\vec{v}\rangle = \vec{v}_i - \hbar\vec{k}_1/M$. This process is repeated at roughly the scattering rate of photons $\gamma_p \sim 1\,\text{MHz}$, resulting in an extremely high cooling rate.

2.1.3 Doppler Cooling of a Cloud in One Dimension

To understand how the Doppler cooling effect described in the last section applies to a cloud of atoms, the excitation parameters of § 2.1.1 must be applied. Recall the detuning $\delta = \omega_L - \omega_0$. With consideration of the Doppler effect, the frequency of the applied electric field that atoms in a cloud experience changes with their signed speed. Thus, detuning becomes dependent on velocity, $\delta(v) \equiv \omega_L - \omega_0 \mp |\omega_D| = \delta \mp |\omega_D|$ where $\mp\omega_D$ is the change in the observed frequency of the laser due to the Doppler effect on an atom moving $\pm v$. Since the probability that an atom is found in the excited state is dependent on δ, this similarly becomes dependent on the velocity, $\rho_{ee} = \rho_{ee}(v)$. Thus atoms in a cloud can be selectively excited based on their velocity class.

This velocity-dependent excitation can be described as a force on atoms in the cloud [4]. For a single laser beam propagating through the gas in the $+z$-direction then reflecting off a mirror and propagating back through the gas in the $-z$-direction, the force on the atoms due to the +/- beam is

$$\vec{F}_{\pm} = \pm\frac{\hbar\vec{k}_L\Gamma}{2}\frac{s_0}{1+s_0+[(\delta\mp|\omega_D|)/\Gamma]^2}. \tag{2.5}$$

The sum of these two forces $\vec{F}_{OM} = \vec{F}_+ + \vec{F}_-$ gives the "optical molasses" force on atoms within the laser beam

$$\vec{F}_{OM} \approx \frac{2\hbar k_L^2 \delta s_0 \vec{v}}{\Gamma[1+s_0+(\delta/\Gamma)^2]^2} \tag{2.6}$$

which can be written $\vec{F}_{OM} = \beta\vec{v}$ where β is the damping coefficient ($\beta < 0$ only for $\delta < 0$, thus cooling is only possible for red detuned light). This velocity-dependent force can be plotted for different velocities as Fig. 2.4.

This velocity-dependent force can be connected to the idea of cooling a gas of atoms by recalling the Boltzmann distribution of speeds in an ideal gas (Fig. 2.5):

$$f(\vec{v}) = \sqrt{\frac{m}{2\pi k_B T}}\exp(-m|\vec{v}|^2/2k_BT) \tag{2.7}$$

where $\vec{v}$ is the 1D velocity of an atom, m is its mass, T is the temperature of the gas, and k_B is the Boltzmann constant. Application of the optical molasses force F_{OM} concentrates the Boltzmann distribution near zero, corresponding to a reduction in temperature.

2.1.4 Laser Cooling of Rubidium

The QSUM lab's current focus is cooling ^{87}Rb. The targeted cooling transition is the D_2 transition between the $5S_{\frac{1}{2}} \rightarrow 5P_{\frac{3}{2}}$ states. The energy difference between

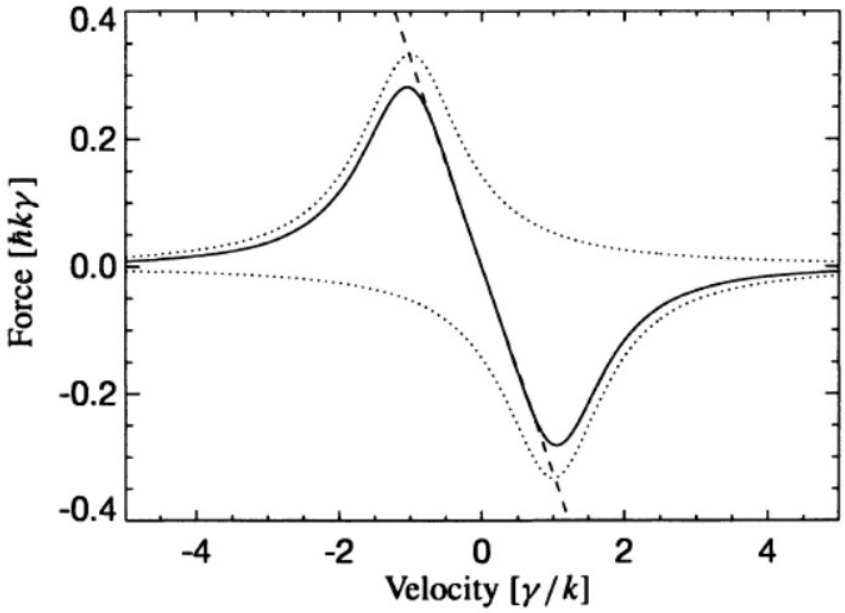

Figure 2.4: Velocity-dependence for one-dimensional optical force on an atom. Dotted lines trace force from beams propagating in each direction, and the solid line is the sum (total force). The dashed line shows how the velocity-dependent force mimics a pure damping force over a restricted domain. Image taken from [4].

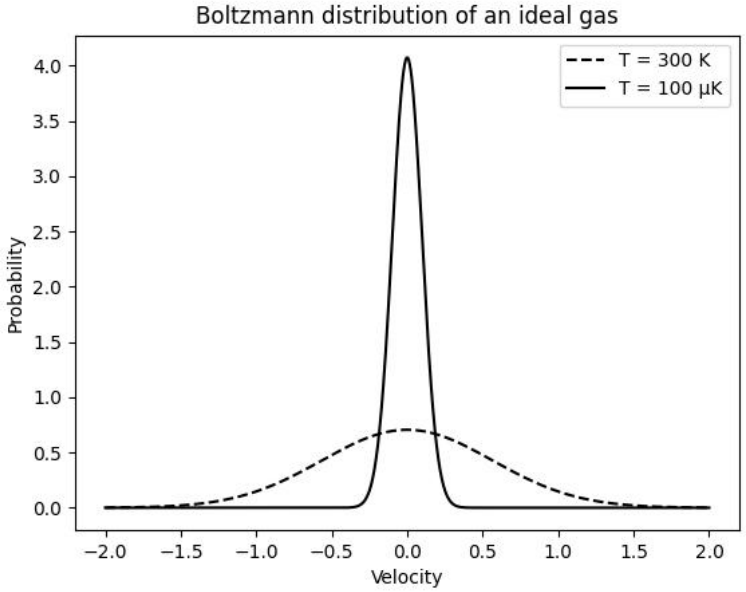

Figure 2.5: Boltzmann distribution in one dimension. For ease of comparison, axes are scaled differently for the two temperature curves: $[v_{100\,\mu\mathrm{K}}]_u = 300[v_{300\,\mathrm{K}}]_u$ and $[P_{100\,\mu\mathrm{K}}]_u = 300[P_{300\,\mathrm{K}}]_u$.

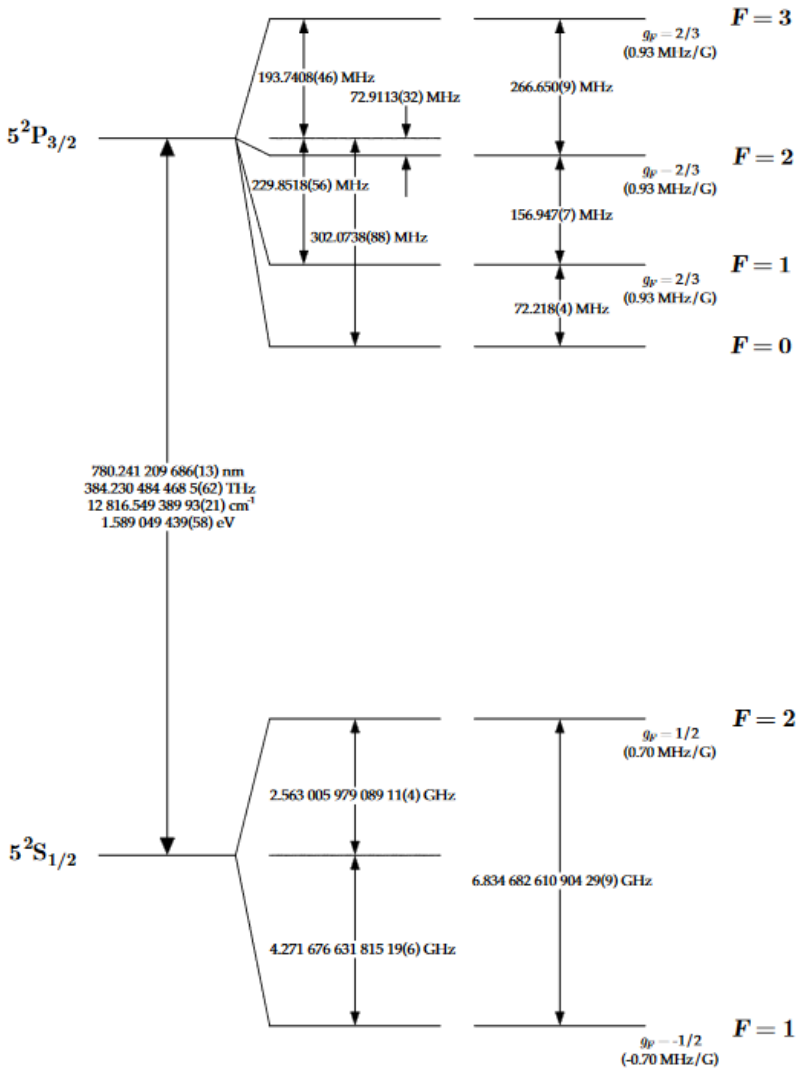

Figure 2.6: Structure of the D_2 transition of ^{87}Rb. Includes electric and fine magnetic states. Image taken from [9].

these two states corresponds to light of wavelength 780 nm (see Fig. 2.6). The lifetime of the excited state has been measured using gas-phase laser spectroscopy as 26.24 ns [8]. Inverting the lifetime gives the decay rate, $\Gamma = 38.1$ MHz. Cooling at the D_2 transition is historically the preferred choice since 780 nm lasers are widely available.

2.2 Optical Trapping and the 2D$^+$-MOT

In § 2.1, the Doppler method of cooling is discussed in detail. However, it is ineffective to trap a cloud of atoms by this method alone. The Doppler method produces a velocity-dependent force for an atom of $\vec{v}$, but this force decreases as $|\vec{v}| \to 0$, hence, slow-moving atoms eventually wander out of the laser beams. Atoms are cooled but are not trapped in a particular region. A position-dependent restoring force is required to maintain atoms in the center of the trapping region.

One method of generating this force is the magneto-optical trap (MOT), described in detail by Raab et al. [10]. Through this method, a magnetic field is applied to induce hyperfine splitting of an atom's energy levels. This can be exploited to produce a trapping force.

In the QSUM lab, two different MOTs are being implemented: the 3D-MOT and the 2D$^+$-MOT . The 3D-MOT confines and cools in 3D, while the 2D$^+$-MOT cools atoms in two transverse directions before pushing them along a third longitudinal axis. This creates a cold jet of atoms that can be efficiently loaded into the 3D-MOT. This thesis focuses on the 2D$^+$-MOT, so special care is taken in describing the trapping region and methods of this type of MOT.

2.2.1 The Magneto-optical Trap

To generate a trapping force using MOT principles, a magnetic field gradient is applied across the trapping region. Consider a hypothetical two-level atom with a ground state $|g\rangle$ in which the total spin $J = 0$ ($M_J = 0$) and an excited state $\langle e|$ in which the total spin $J = 1$ ($M_J = -1, 0, 1$). If the external magnetic field is zero, the magnetic states corresponding to $M_J = -1, 0, 1$ are degenerate. However, in an applied magnetic field $\vec{B}(z) = B_0\vec{z}$, the degeneracy is broken by the Zeeman effect, and the magnetic states are split by an amount $\Delta E_J = M_J g_J \mu_B |\vec{B}(z)|$ where g_J is

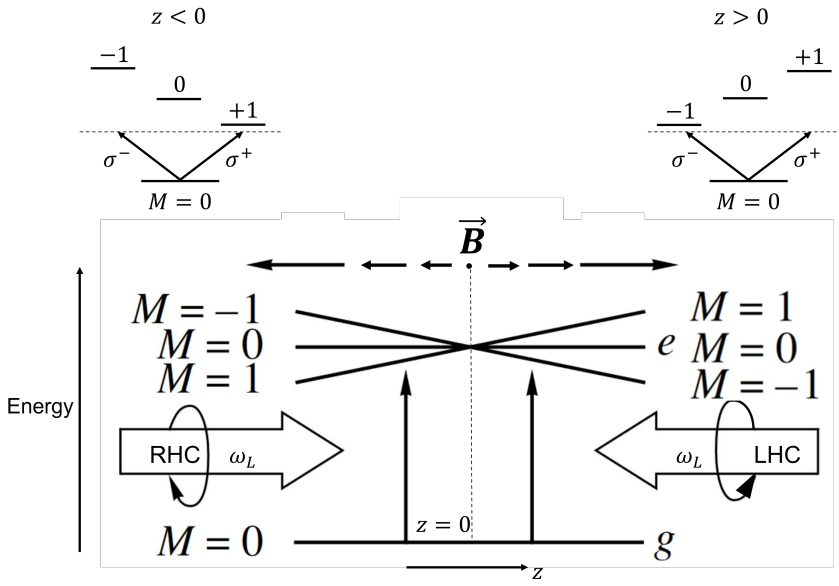

Figure 2.7: The magnetic field gradient across the trapping region induces hyperfine splitting in the energy level structure of a two-level atom generating a position-dependent force as described in the text.

a g-factor and μ_B is the Bohr magneton [5, 10, 11]. Fig. 2.7 illustrates this effect for a $J = 0 \rightarrow J = 1$ atomic transition.

Now apply a detuned laser (as described in § 2.1) of frequency ω_L and right-handed circular (RHC) polarization from the $-\hat{z}$ direction. Due to the conservation of angular momentum between the atom and the exciting photon, atoms in the $M_J = 0$ ground state will preferentially absorb light from the RHC beam on the left ($z < 0$) of the zero-point in the field. These correspond to the σ_+ transitions shown. Apply a similarly-detuned laser of left-hand circular (LHC) polarization from the $+\hat{z}$ direction to double this effect. A new definition of the detuning $\delta_\pm$ must be applied since the targeted transitions now change with position: $\delta_\pm = \delta(v) \pm \mu' B/\hbar$ where $\mu' = (g_e M_e - g_g M_g)\mu_B$ is the effective magnetic moment for the targeted transition. The force on the atom is given, as before, by Eq. 2.5 with $\delta_\pm$ newly defined as above. Written out, this looks like

$$\vec{F}_{MOT,\pm} = \pm \frac{\hbar \vec{k}_L \Gamma}{2} \frac{s_0}{1 + s_0 + [(\delta \mp |\omega_D(\vec{v})| \pm \mu' B(\vec{r})\hbar)/\Gamma]^2}. \tag{2.8}$$

As long as the effects of the Doppler shift and the new so-called "Zeeman shift" (so named because it operates on the Zeeman splitting of the upper state) are small compared to the detuning itself, the force equation can be expanded and summed as above to find

$$\vec{F} = \beta\vec{v} - \kappa\vec{r} \tag{2.9}$$

where $\kappa = \beta\mu' B_0/\hbar k_L$ acts as a spring constant. This is readily scaled up to three dimensions by the application of four more detuned, polarized laser beams along the other two axes.

2.2.2 Purpose of the 2D$^+$-MOT

To trap atoms in a 3D-MOT, they must be coaxed into the trapping region. It is possible to do this using pressure differentials between a source cell and the trapping region, but this is slow compared to other methods. This pressure differential method also tends to select fast atoms to enter the trapping region, which are more difficult to trap.

There exist several solutions to this problem including the Zeeman slower [12], the LVIS [13], and the laser-free slow atom source [14]. However, perhaps the simplest solution is the 2D$^+$-MOT [15]. This method traps atoms in two dimensions and pushes them into the 3D-MOT in the third.

There are two conceptual components of the 2D$^+$-MOT, the 2D-MOT (similar to the 1D-MOT described above but applied in the two transverse dimensions) and the push beam laser which applies a force to atoms along the third longitudinal axis of the trap. These are treated separately below (as they are separable physical phenomena).

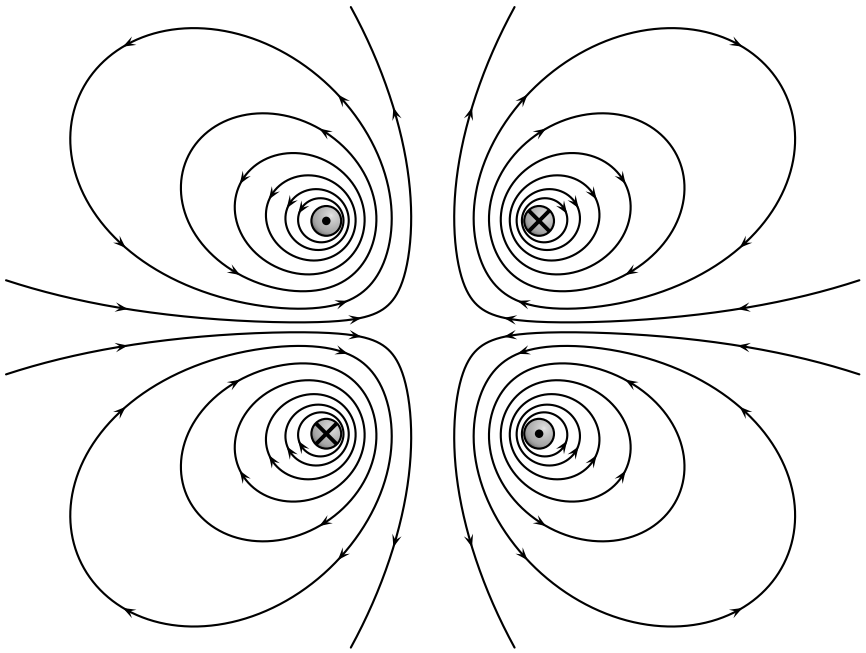

Figure 2.8: Cross-section of the quadrupole magnetic field required for trapping atoms in two dimensions.

2.2.3 Magnetic Field Design

As in the case of the 1D-MOT described above, it is necessary to generate a magnetic field gradient across the trapping region. However, for the 2D-MOT, a two-dimensional gradient is necessary. That is, there must be a gradient in both x and y to imprint 2D-positional information on a particle. The magnetic field structure in the transverse plane is shown in Fig. 2.8.

There exist two widely-used methods for generating such a magnetic field [16]. The first method uses a configuration of four permanent magnets to produce the desired field. The permanent dipole method benefits from being a solid-state system — no current supply is required to generate or regulate the field. The second method applies the magnetic fields generated in loops of current-carrying wire to produce the same field. This electro-magnet method benefits from higher user control — currents can be tuned to modify and optimize the magnetic gradient (and the corresponding MOT force). In addition, the field can be rapidly switched off to ensure it does not

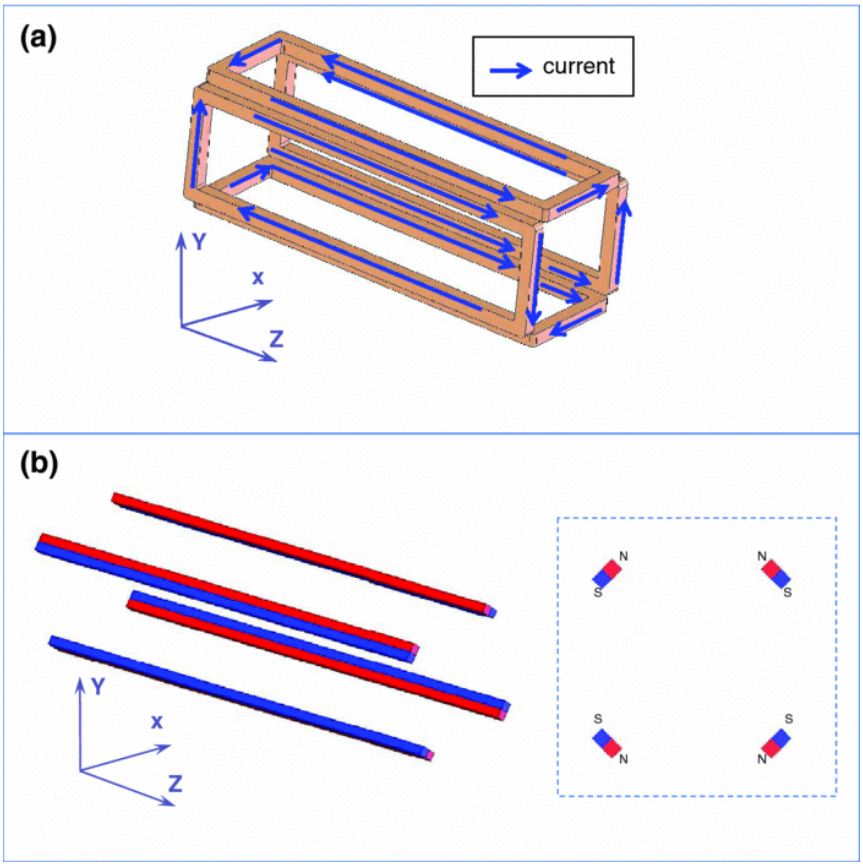

Figure 2.9: Methods of generating 2D-MOT field: a) Current-carrying coils, b) Permanent dipole magnets. Image taken from [16].

interfere with other components.

The QSUM lab uses the second method to generate its $2D^+$-MOT to remove the trapping force on atoms in the MOT very quickly. This allows the flow of atoms into the 3D-MOT to be controlled precisely which is useful for certain experiments.

To implement this electro-magnet, the QSUM lab designed and implemented a 3D-printed housing (see Fig. 2.10) and wound it with coils of wire in the anti-Helmholtz configuration [17, 18]. In this configuration, current flowing through opposing coils flows in opposite directions to produce the desired magnetic field of $35\,\mathrm{G\,cm^{-1}}$.

In three dimensions, the $2D^+$-MOT trapping region is an ellipsoid with two axes being symmetrical and the third being elongated (see Fig. 2.11). This is commonly

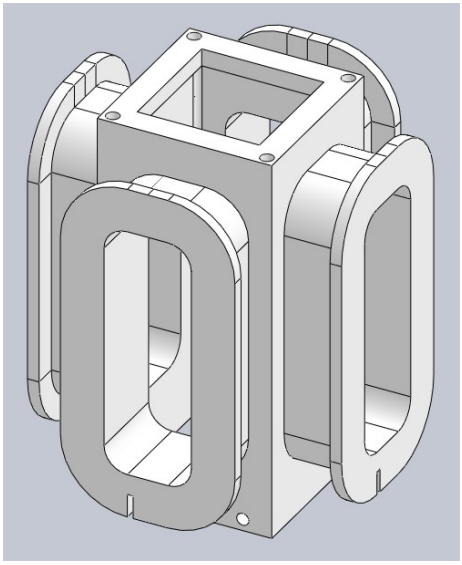

Figure 2.10: Solidworks Model of $2D^+$-MOT electro-magnet housing.

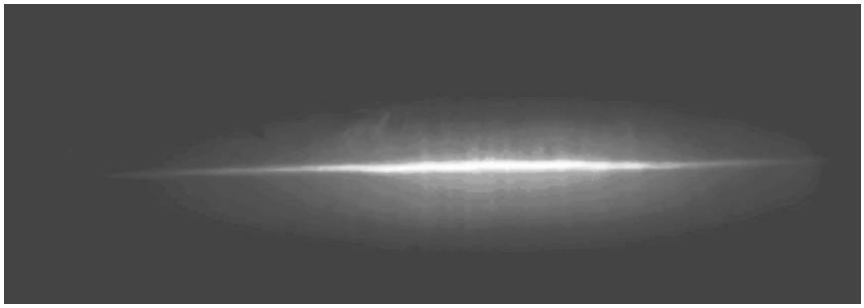

Figure 2.11: Image of trapped atoms in a 2D-MOT. Note the cigar shape. Not from the QSUM lab. Image taken from [19].

called a "cigar-shaped trap."

2.2.4 Push Beam

The elongated axis in Fig. 2.11 does not require a laser beam in the pure 2D-MOT setup. Trapping is performed along the transverse directions only. However, in the QSUM lab, a third laser is applied along the longitudinal axis. At one end of this axis, a small pinhole is placed so that atoms can escape into the 3D-MOT, as shown in Fig. 2.12. This push-beam laser is detuned similarly to the others but is not reflected. Thus, only the F_+ force of Eq. 2.5 is applied, and affected atoms are pushed into the 3D-MOT.

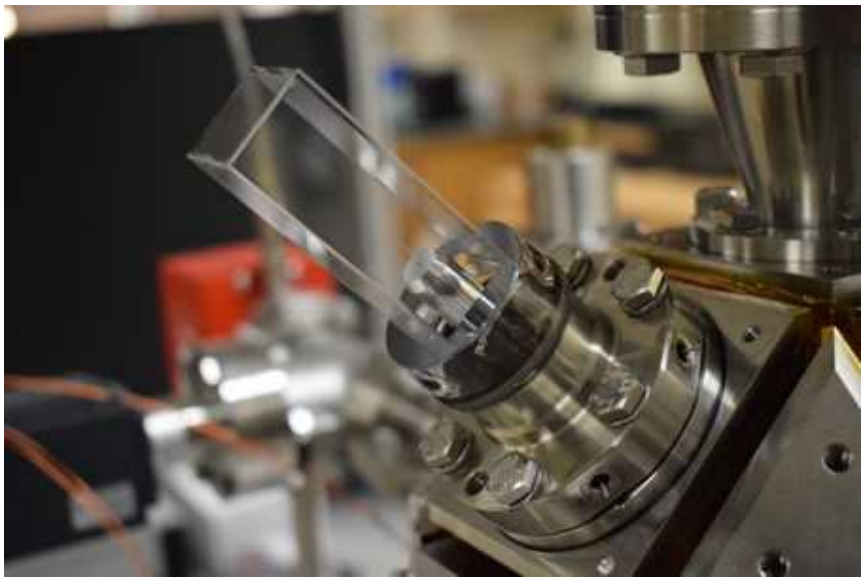

Figure 2.12: Photograph of the commercial glass cell with integrated Rb dispensers and pinhole from Cold Quanta used in the $2D^{+}$-MOT in the QSUM lab. Courtesy of Kamal Shalaby, QSUM lab.

Chapter 3

Optical Requirements of the $2D^+$-MOT

This chapter gives an overview of the laser cooling apparatus's laser system. Particular care is taken further in the chapter to discuss the optical components specific to the $2D^+$-MOT, including the optical switch used to quickly shut off the system, the fiber splitters, and the beam delivery system.

3.1 Overview of Laser System

This section provides a broad description of the laser system. A block diagram of portions of the system relevant to this project is shown in Fig. 3.1.

The system consists of a fiber-coupled diode laser operating at 1560 nm (Elbana model EP1560-5-NLW-B26-200FM) with a linewidth of 200 kHz and maximum output power of 8 mW. 1560 nm light is used instead of light of the transition frequency (780 nm) because equipment such as optical amplifiers are more developed and widely available at this wavelength. This diode seeds an erbium-doped fiber amplifier (Lumibird model CEFA-C-PB-HP), which can boost the optical power up to 5 W. For the experiments described here, the amplifier is operated in a low-power configura-

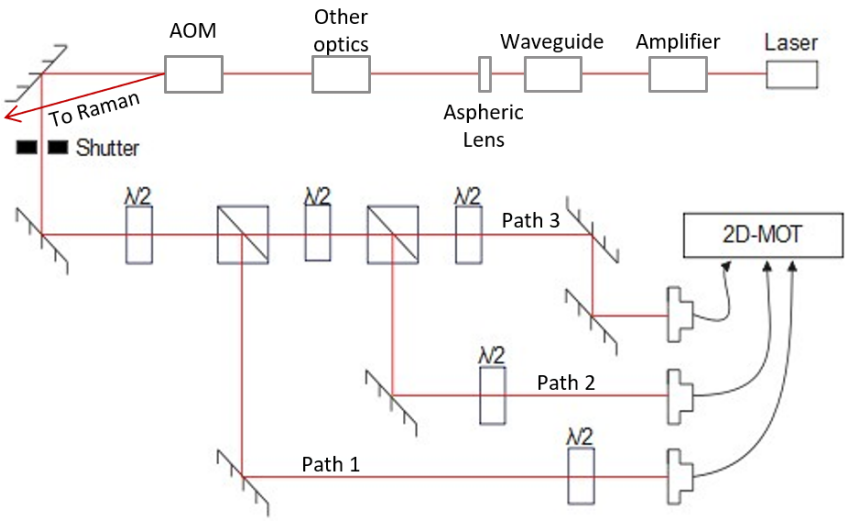

Figure 3.1: Beam-splitter Path Optical Block Diagram.

tion such that it produces only 500 mW. The output of the amplifier is then sent to a periodically-poled lithium niobate crystal waveguide (Covesion model WGCF-1560-40) that doubles the optical frequency/halves the wavelength to 780 nm through a non-linear optical process called second-harmonic generation. Light at 1560 nm enters the waveguide by fiber where it is converted to approximately 100 mW at 780 nm. This light exits the waveguide in free space where it is collimated by an aspheric lens and sent through a series of optics mounted on a rigid optical table. These and free space optics include a series of half wave plates, polarizing beamsplitter cubes, irises, and mirrors that are irrelevant for this work. In general, the purpose of these "other optics" (as shown in Fig. 3.1) is to divert light to different parts of the apparatus. About 15 mW of light of wavelength 780 nm makes it to the AOM labeled in Fig. 3.1, which is taken as the start of the fiber-coupled pathway this thesis focuses on.

A method of matter-wave interferometry known as Raman interferometry is planned as a part of this experimental apparatus (see i.e. [19] or [15]). This requires an intense source of light, so using the first-order diffraction generated by the AOM is a natural choice. Diffraction occurs only when the AOM is in operation (i.e when

the trap is turned off), and provides $\sim 80\%$ of the intensity of the original beam.

As described in § 2.1, laser cooling utilizes two energy levels within an atom. The transition of ^{87}Rb targeted by the experiment is weakly coupled to other states that reduce the efficiency of the trap. Thus, a repumping laser is used to ensure atoms continue cycling on the cooling transition between the target states. This laser will need to be coupled and characterized much like the main cooling laser.

3.2 Cooling Laser Beam Profile

As discussed in § 2.2, the trapping region for the 2D$^+$-MOT is not spherical. In fact, the sides of the glass cell for the 2D$^+$-MOT are rectangular (see Fig. 2.12). With the shape of the cell in mind, it is desirable to generate a laser beam profile that is not circular but is instead elliptical to capture the widest number of particles possible.

The beam exits the laser with a spatial intensity profile described by a small, circular Gaussian distribution. To fit the requirements described above, the beam should have an elliptical intensity profile with an aspect ratio similar to the glass cell and magnetic field gradient. To achieve this aspect ratio, the beam is stretched along one axis using an anamorphic prism pair (APP) (see Fig. 3.2) and then expanded along both axes using a Galilean telescope as a magnification device (see Fig. 3.3).

The APP stretches the beam along one axis while maintaining its dimensions along the other. It does this by diverting the path of incident light according to its initial position along the first prism. As shown in Fig. 3.2, the lower end of the beam is diffracted first and moves further in free space between the prisms than the upper end. This leads to a beam elongated along one axis, as desired. The ThorLabs PS875-B anamorphic prism pair, which doubles the profile along one axis, is used in the QSUM lab.

The Gallilean telescope uses one concave lens which bends the path of the light

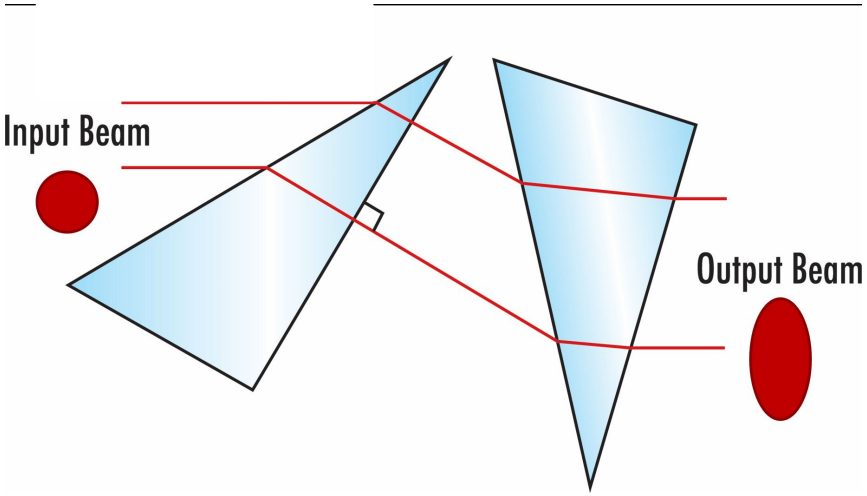

Figure 3.2: Anamorphic prism pair diagram. Taken from [20].

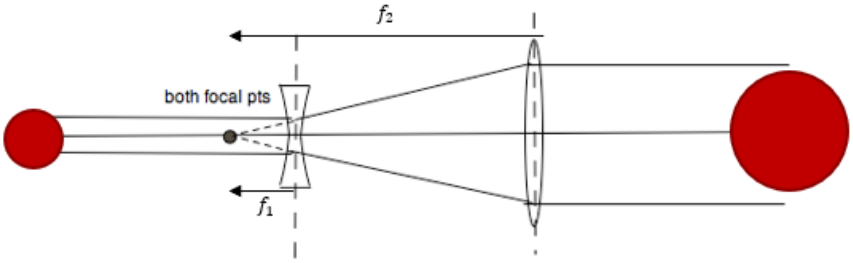

Figure 3.3: Gallilean telescope for magnifying the beam size. Beam size magnification follows relationship $M = \frac{f_2}{f_1}$. Taken from [21].

away from the centre in all directions and one convex lens which focuses the light back into a collimated beam, as shown in Fig. 3.3. Magnification follows from the law $M = \frac{f_2}{f_1}$. In the QSUM lab, the lenses used have focal lengths $f_2 = 125\,\text{mm}$ and $f_1 = 25\,\text{mm}$. These result in a magnification of factor $M = 5$. The focal points of both lenses must be collocated for this scheme to be effective. The advantage of this scheme over two convex lenses is that it saves space. This allows a more compact setup.

The combination of the APP and Galilean telescope provides an elliptical beam profile with $1/e^2$ diameter $28.79\,\text{mm} \times 13.80\,\text{mm}$. This is an ideal starting point for the glass cell's dimensions (see [18]).

Although these optics could be arranged in either order in theory, it is better in practice to place the APP before the magnifier since the smaller beam size is easier to manipulate. Thus, in the QSUM lab, the optics are arranged according to Fig. 3.4.

3.3 Optical Splitting Path

The $2D^+$-MOT requires lasers from three different directions — two trapping beams along the x- and y-axes and a third push beam along the z-axis. The diode laser used by the QSUM lab produces a single beam, so, to satisfy these requirements, the beam must be split in three. This is done using two polarizing beamsplitter (PBS) cubes and two half-wave plates ($\lambda/2$-plates). PBS cubes consist of two triangular prisms cemented together according to Fig 3.5. The base of one prism is coated to reflect horizontally-polarized light and transmit vertically-polarized light. By this method, a single incident beam of light can be split based on its incident linear components of polarization.

To make effective use of the PBS cube, the polarization of the incident light must be linear and under the control of the experimenter. There are a few methods in use

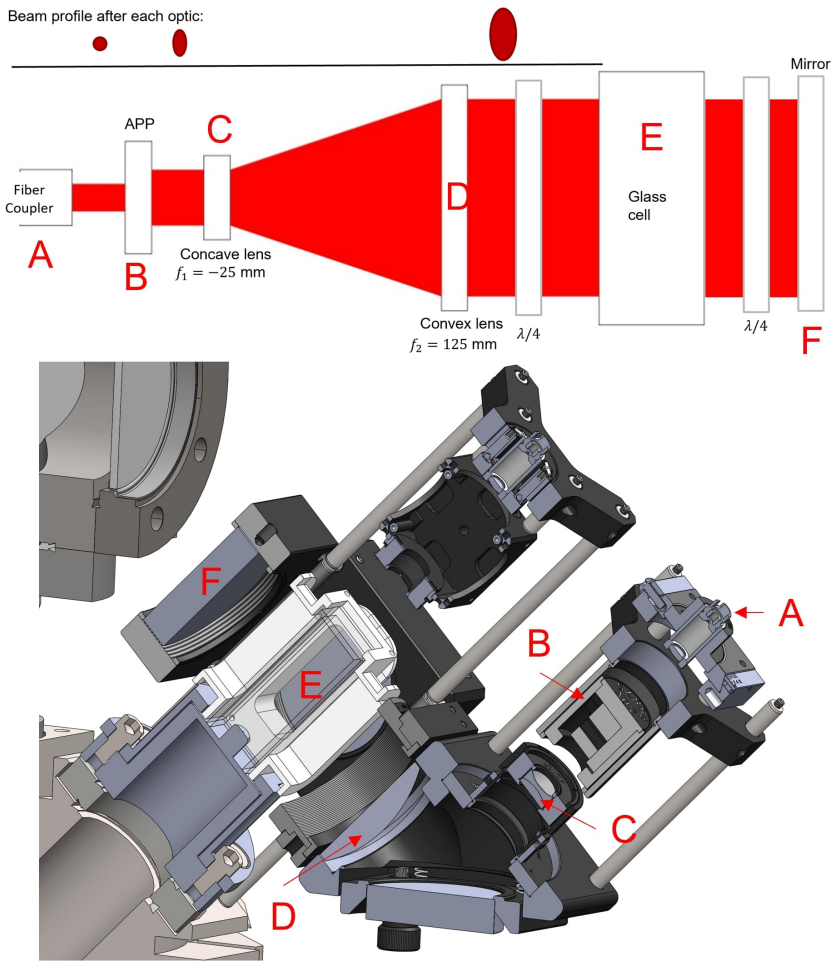

Figure 3.4: Optical block diagram showing placement of optics used to optimize the beam profile for the 2D$^+$-MOT and corresponding placements in Solidworks 3D model.

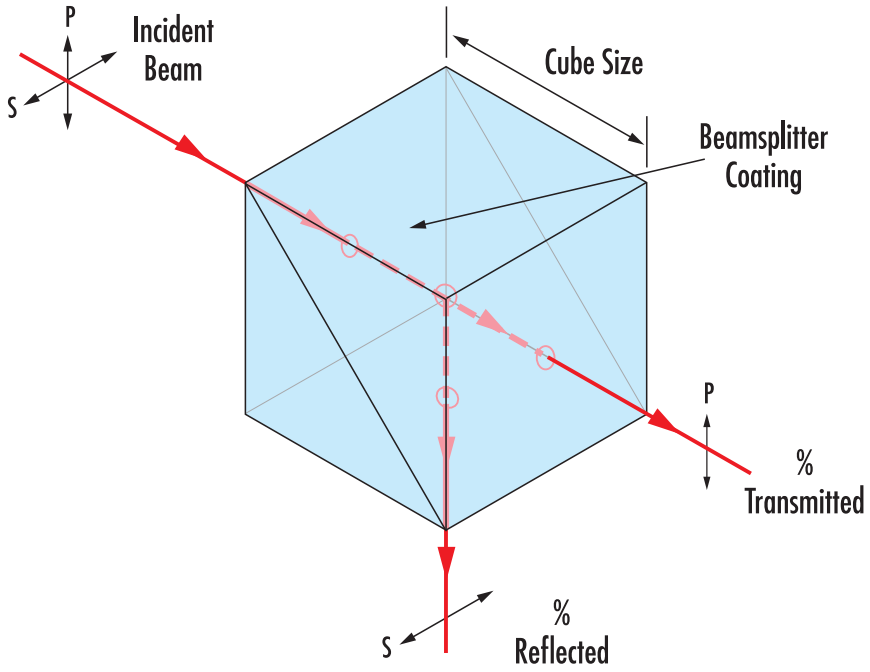

Figure 3.5: Polarizing beamsplitter cube diagram. Image taken from [22].

for changing the polarization of a laser beam, but the method used in the QSUM lab involves passing the beam through a $\lambda/2$-plate (see Fig. 3.6). A $\lambda/2$-plate consists of a birefringent material with a fast axis and a slow axis. Incident light polarized along the fast axis remains unchanged through the optic; light polarized along the slow axis is retarded by one half-wavelength resulting in a 180° phase shift between the polarization components exiting the fast and slow axes. This property can be used to rotate the plane of linear polarization, allowing for control of the amount of light reflected and transmitted by the PBS.

By configuring a series of PBS cubes and $\lambda/2$-plates as in Fig. 3.1, it is possible to split an incident beam into three outputs to be used in the $2D^+$-MOT.

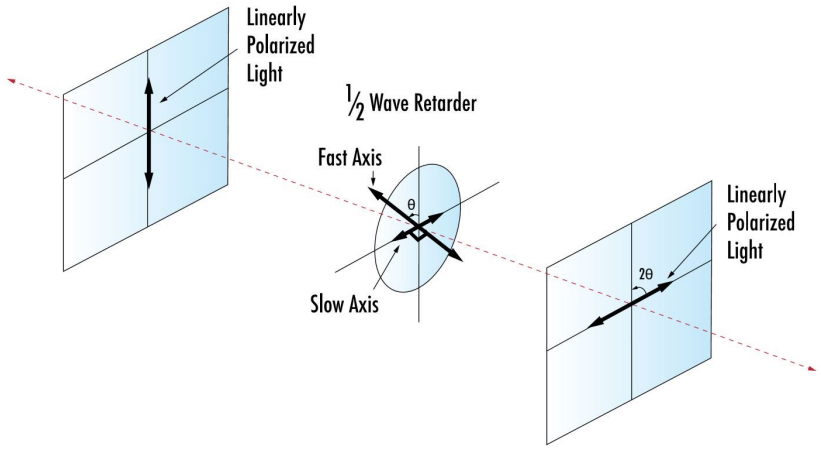

Figure 3.6: Half-waveplate diagram. Taken from [23].

3.4 Mechanical Shutter and Acousto-Optic Modulator

To control the amount of light entering the $2D^+$-MOT setup, the QSUM lab employs an acousto-optic modulator (AOM) and a mechanical shutter.

An AOM consists of a quartz crystal that changes its index of refraction under pressure and a piezoelectric transducer (PZT) (see Fig. 3.7). By applying a radio frequency signal to the PZT, acoustic pressure waves can be generated in the material. The spatially varying index of refraction induces a diffraction grating in the material. Then, incident light is separated according to the principles of diffraction.

Notably, the intensity of light at an angle θ from the zero-order (undiffracted) beam can be described according to the Fraunhofer approximation

$$I(\theta) = I_0 \left(\frac{\sin\left(\frac{d\pi}{\lambda}(\sin\theta \pm \sin\theta_i)\right)}{\frac{d\pi}{\lambda}(\sin\theta \pm \sin\theta_i)} \right)^2 \tag{3.1}$$

where I_0 is the intensity of the incident light, d is the separation of induced diffraction grating in the AOM, λ is the wavelength of the incident light, and θ_i is the angle between the induced diffraction grating and the incident light.

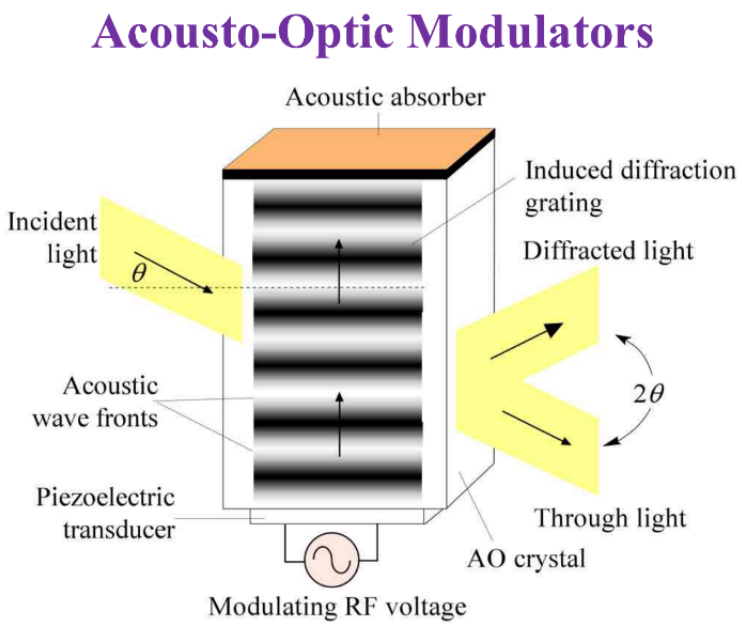

Figure 3.7: AOM diagram. Image taken from [24].

Examining Eq. 3.1, it is possible to select certain θ to be intensity minima by carefully choosing the angle of incidence θ_i. Thus, it is possible to use the diffraction grating induced in the AOM as an on/off switch by selecting θ_i such that $I(0) = 0$. The first zero of $\frac{\sin x}{x}$ occurs at $x = \pm\pi$, so at $\theta = 0$, $\pm\frac{d\pi}{\lambda}\sin\theta_i = \pm\pi$. This implies that if θ_i is chosen as $\arcsin\left(\frac{\lambda}{d}\right)$, the intensity of the zero-order beam goes to 0 when the AOM is in operation.

In practice, this on/off switch is imperfect since the laser beam is not a point source (i.e. the beam itself covers some extent of θ, and there is no optimization of θ_i that perfectly corrects for this) and perfect alignment is not achievable. Generally, AOM switches can be expected to diffract about 80% of the light away from the zero-order path. Thus, to remove the final 20%, the QSUM lab employs a mechanical shutter.

The system appears redundant at first glance: if the shutter cuts out 100% of the light, why use the AOM at all? There are two main reasons for using the AOM: first, it is much faster than a mechanical shutter. The first-order diffraction has a

high extinction ratio, so pulses of temporal width $\sim 100\,\text{ns}$ are possible. Modulating the light in this way during the operation of the $2D^+$-MOT can lead to interesting results. Second, running the AOM at variable radio frequency power yields variable transmittance, allowing the AOM to be used as a dynamic optical attenuator.

However, the main purpose of the AOM is to generate a signal through its first-order diffraction for Raman interferometry. As discussed below, Raman interferometry allows measurements of the $2D^+$-MOT's trapping capabilities.

The shutter is a simple system compared to the AOM; it takes a button press or a logic signal as input and opens or closes based on this input. When open, 100% of the incident light passes through. When closed, all light is blocked by the physical barrier and 0% passes to the rest of the system.

3.5 Fiber-optic Couplings

The QSUM lab uses 780 nm single-mode polarization-maintaining (PM) fiber-optic cables to transport light between optical systems. These operate on the principle of total internal reflection. The cladding and core of a fiber-optic cable (see Fig. 3.8) are constructed of materials with different indices of refraction so that when an analysis of the system is applied using Snell's law ($n_I \sin\theta_I = n_R \sin\theta_R$, where I denotes the incident material and R the material the light reflects off of), it's possible to choose an angle of incidence θ_I such that all light is fully reflected.

Total internal reflection occurs for any $\theta_I > \theta_C = \sin^{-1}(n_R/n_I)$. Typically, the core has $n_I \sim 1.5$ and the cladding has $n_R \sim 1.4$, implying $\theta_C \approx 69^\circ$ (relative to the normal of the surface).

Examining now the input of the fiber, the numerical aperture (NA) is defined as $NA = n \sin\theta_{max}$, where n is the refractive index of the medium between the optical element and the object being imaged ($n \sim 1$ for air) and θ_{max} is half the acceptance

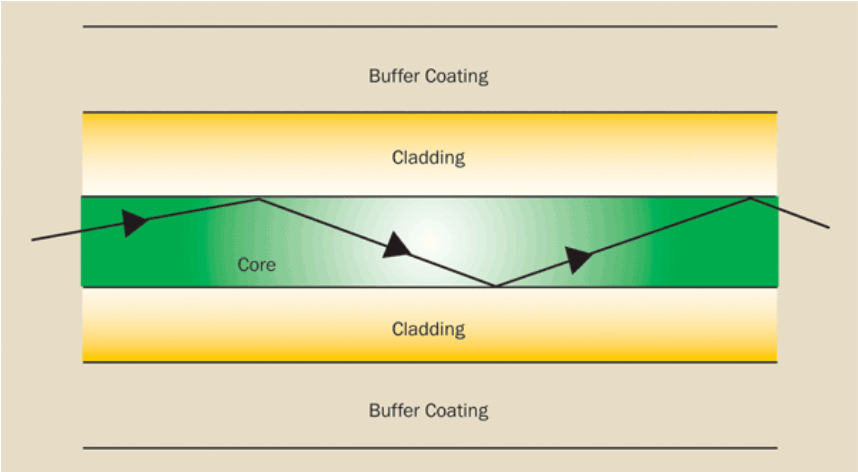

Figure 3.8: Fiber-optic cable diagram. Image taken from [25]

angle of the optic. For the fiber-optic cable being examined, the acceptance angle is the complement of the critical angle $\theta_{max} = 21°$. This implies $NA \sim 0.3$ for the fibers used. Single-mode fibers are designed so that the NA is small such that only one spatial mode can exist inside.

However, such a small NA requires precision alignment of the input beam. This is performed using a collimator (see Fig. 3.9). These collimators are sold pre-assembled in collimation packages which allow for adjustment of the z-axis separation of the lenses (corresponding to z-axis position of the focus) and tip/tilt xy-translation of the focus. In theory, with perfect alignment of the focal point of the collimator and the lens, very high transmittances are possible.

In practice, a transmittance of about 60% is achievable if the input beam profile is well-matched to the fiber's NA. Achieving this efficiency requires an iterative process of adjusting the tips and tilts of various optics (for full details, see [18]). Alignment precision in the mrad range is required to achieve efficient coupling.

Once alignment is achieved, it becomes important to study how well it can be maintained. Anything from air currents to temperature to the moisture content of the air can cause minute changes in the angle of incidence of the beam on the fiber collimator, impacting the transmittance efficiency. Study of such instabilities is a

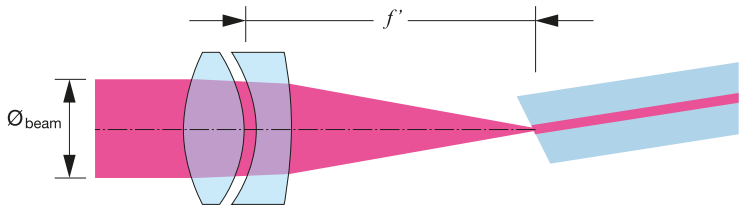

Figure 3.9: Fiber Collimator Diagram. Focus f' can be manipulated by changing the distance between lenses. Image taken from [26].

focus of the this thesis (see § 4.3.2).

Chapter 4

Characterizing the 2D$^+$-MOT Optical Paths

This chapter discusses the characterization of three optics in the fiber-coupled optical delivery system. The order follows the path of the laser shown in Fig. 3.1, beginning with the AOM, then the mechanical shutter, and finally the stability of the fiber-optic couplings.

4.1 AOM

The AOM is intended to modulate the power to the 2D$^+$-MOT quickly and provide power for a Raman interferometer. It is therefore important to characterize its efficiency in shifting light from the 0$^{\text{th}}$-order path (coupled to the 2D$^+$-MOT) to the first-order path (coupled to the Raman interferometer).

The first-order diffracted beam contains the majority of the intensity lost from the 0$^{\text{th}}$-order. Thus, to characterize the AOM, it was deemed acceptable to measure the light just after the AOM before it is turned on and the output of the first-order beam after it is turned on.

The power of the 0$^{\text{th}}$-order beam using a Thorlabs power meter before the

	Mean (ms)	Deviation (ms)
Rise delay (δt_{rise})	5.4	0.2
Rise time (Δt_{rise})	1.15	0.03
Fall delay (δt_{fall})	5.2	0.2
Fall time (Δt_{fall})	0.98	0.03

Table 4.1: Table of shutter timings including mean average value and deviation characteristics for a dataset of $N \approx 100$.

AOM was turned on was 56.6 mW. The power of the first-order diffracted beam was measured (with the AOM on) as 44.8 mW. The efficiency, then, was $P_i/P_f = 79.1\%$. This falls in line with the expected value for similar models of AOM ($\sim 80\%$).

4.2 Mechanical Shutter

The speed with which the system can be turned on and off is an important characteristic determined by the optical splitting path. As discussed in § 3.4, the AOM and shutter are used in tandem to first significantly reduce light input to the $2D^+$-MOT, then cut it altogether. The time the AOM takes to switch on and off is nearly instantaneous compared to the shutter, so the shutter acts as a bottleneck and is the component to characterize.

There are two important aspects of the shutter to characterize: the speed at which the shutter closes, Δt, and the delay δt. Δt is the amount of time between when the shutter begins cutting off light and when it is completely closed. δt is the delay between when the shutter is triggered and when it begins to cut off the light.

When examining the delay δt, the standard deviation is more important than the value itself. If the deviation is low, it is trivial to trigger the shutter to close δt before the experiment requires it to close. It becomes less trivial if δt changes significantly between runs.

To measure these characteristics, a system of testing was devised involving a function generator (Stanford Research Systems model DS335) and a power meter

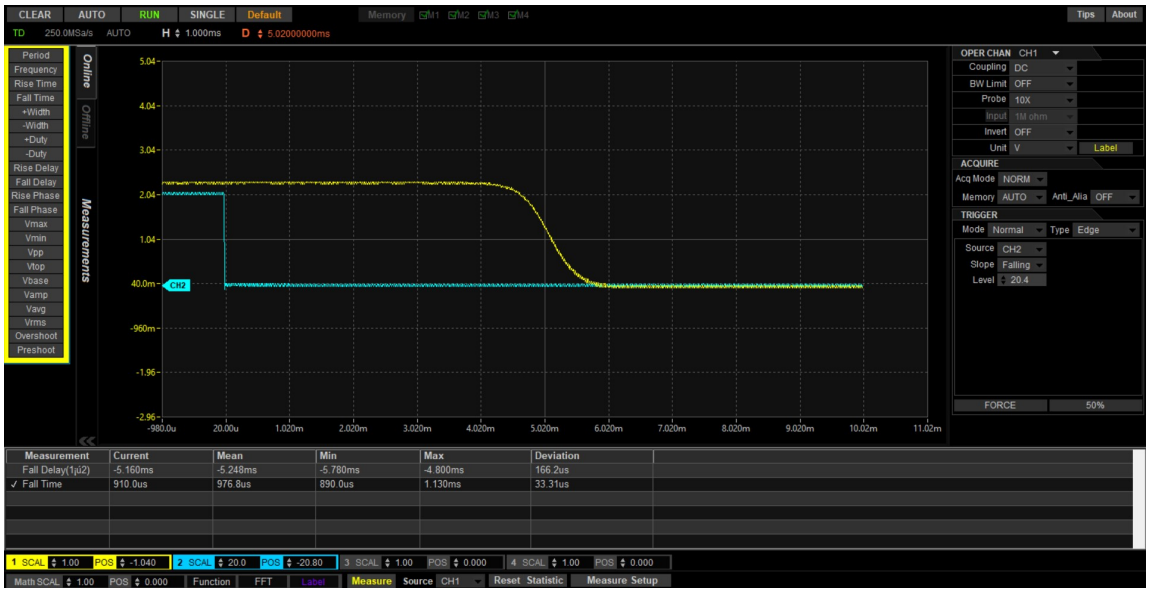

Figure 4.1: Ultrascope software displaying oscilloscope output during mechanical shutter test. The blue line indicates the TTL signal from the function generator. The yellow line indicates optical power measured with a Thorlabs power meter.

(Thorlabs model PM100D). The function generator was connected to the TTL control of the shutter. A power meter was placed facing the opening of the shutter so that the laser was incident upon its detecting surface when on. The output of the power meter and the function generator were coupled to an oscilloscope. The oscilloscope output to Ultrascope software on a lab PC which averaged the data for the length of the test and gave variance statistics (see Fig. 4.1).

Two tests were conducted on the shutter system: the first (second) triggered on a rising (falling) signal from the function generator. For each test, the function generator was set to a period of 2 s. For the first 0.5 s voltage was high (corresponding to the shutter being open). This was followed by 1.5 s of low voltage (with the shutter closed). The system was allowed to run for 5 min before the averaged data was recorded.

A table of data is presented in Tab. 4.1. These data are deemed acceptable for QSUM's purposes. Experiments are expected to last on the order of 100 ms, while the fall/rise time are of order 1 ms, so the problem regions in data collection will

last only about 2% of the total data-collection region. The deviation in the fall and rise delay are about 5% of the fall and rise delay times, meaning the delay can be approximated quite closely as its expected value (so the mean delay times can be used to send the shutoff-signal early enough to close the shutter when desired).

4.3 Fiber-optic Splitter

The 1×3 fiber-optic splitter is at the end of the free-space optical path of the cooling laser system. It transports and spatially filters light to the optical hardware discussed in § 3.3 used to cool and push in the $2D^+$-MOT. These are important to characterize as they are the final region of the optical path before the beam profile is shaped and aligned on the atoms.

There are three important aspects of the fiber-optic couplings to characterize. The first, the efficiency, is the power maintained from the input to the output and is usually expressed as a percentage. The second is the stability of the system. That is, how well the efficiency is maintained over time. The third is the polarization, which is beyond the scope of this project but will be characterized during Summer of 2023. The methods and results achieved in characterizing the first two are discussed below.

4.3.1 Efficiency

The efficiency of the system changes regularly, so must be adjusted and maintained before every use of the path. Changes in efficiency can come from a range of factors, including shifts in temperature changing the microscopic shape of optics and misaligning the light; order arcsecond shifts in alignment of the optics caused by the motion of experimenters in the lab, and changes in aircurrents bending the light from its intended path being a few. The methods of adjustment are discussed in § 3.5. Once the coupling is complete, the power of the laser beam at the input and

Path #	Input (mW)	Output (mW)	% Efficiency
1	4.69	3.07	65.5
2	5.09	3.27	64.2
3	7.37	4.10	55.6

Table 4.2: Example table of input and output power along with coupling efficiency (February 23, 2023).

Date	Path 1	Path 2	Path 3
14/02/23	72.7	70.2	58.9
15/02/23	69.5	69.1	54.1
22/02/23	58.6	59.6	57.8
23/02/23	65.5	64.2	55.6
Average	66.6	65.8	56.6
S. Dev.	6.1	4.9	2.2

Table 4.3: Coupling efficiencies (%) measured just following alignment by date.

output is measured using a Thorlabs power meter (model PM100D, Ge photodiode S122C). These are noted after each adjustment for each path as in Table 4.2. The efficiency is determined by the simple formula

$$\% \text{ efficiency} = \frac{P_{\text{out}}}{P_{\text{in}}} \times 100\%. \tag{4.1}$$

The coupling efficiencies must be adjusted and recorded each time the path is used, so Table 4.3 can be generated as a conglomerate of the data recorded. Examining the average coupling efficiency of each path, the first two paths appear to have a higher efficiency than the third. The first two paths also have a higher standard deviation (calculated as the standard deviation in the population, $s = \sqrt{\frac{1}{n-1}\sum_i (x_i - \bar{x})}$) than the third.

Examining first the difference in averages, there are a few possible explanations. First, the fiber-optic cable may simply need cleaning, polishing, or replacing. A dirty or scratched fiber-optic cable can significantly reduce the maximum power transfer of which the system is capable. This can be tested by direct inspection with a microscope, or by replacing the cable with an identical model and finding the new

optimal efficiency. Second, the alignment of the third path may be fixed at a local maximum rather than the global maximum. There are three degrees of freedom when aligning the beam, and the alignment curve in two of the dimensions has multiple peaks. Thus, it can be difficult to determine whether the "true" maximum has been reached. This should be investigated further once the cable has been tested. Third, the collimation package could require cleaning or replacement.

Next, the difference in standard deviations. This is easily explained; when realigning the system, achieving the maximum possible alignment was not always the goal. To speed up the alignment process, often only two degrees of freedom were adjusted (the xy tip-tilt adjustments and the fiber collimator). It would be possible to adjust the system in all five degrees of freedom (xy beam translations, xy tilts, and z-axis focus), and find similar efficiencies each time, but this would greatly increase the time investment in aligning the system for little gain. There is no reason to expect the maximum achievable efficiencies ($\sim 72\%$) to have changed.

4.3.2 Stability

Another aspect of the fiber-optic splitter path to characterize is the stability of the system over long periods. To measure this, a system of three photodiodes was constructed and coupled to the outputs of the three fibers shown in Fig. 3.1. Notably, the fibers were not recollimated or focused on the photodiodes due to a lack of equipment: the fiber output was simply connected to a pinhole facing the photodiode. This method of coupling could unfortunately result in a slight loss of power to light shining outside the active area of the photodiode. The first-order diffracted beam of the AOM was measured using a Thorlabs power meter to isolate changes in the laser system as a whole from drifts in each path.

The photodiodes used to measure output were each constructed according to Fig. 4.2, which is a low-noise trans-impedance amplifier. This circuit amplifies the

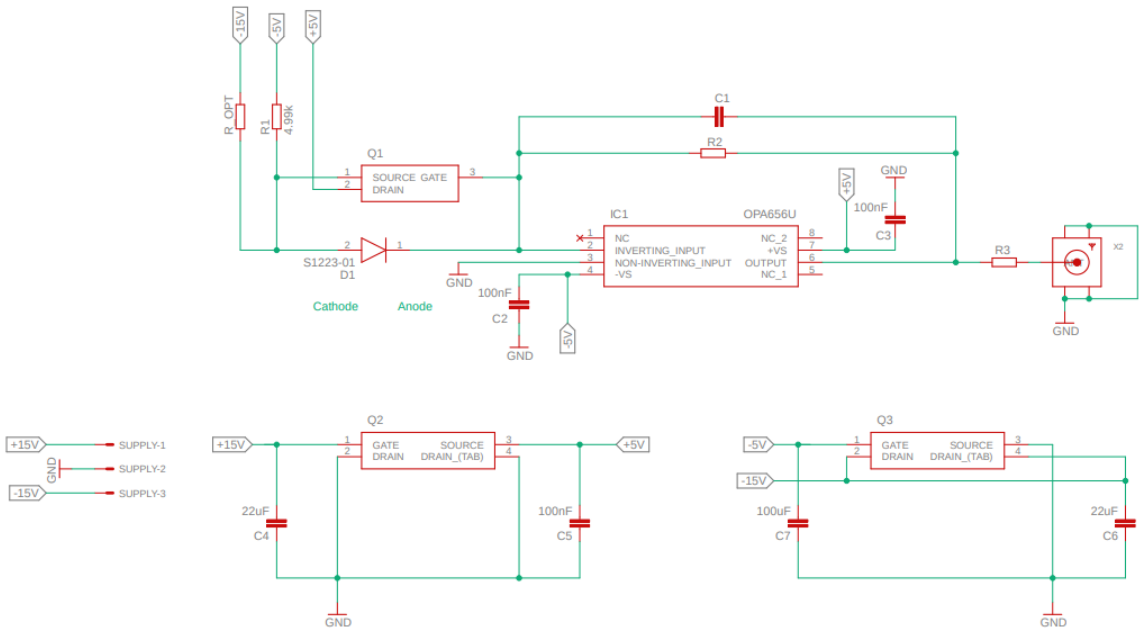

Figure 4.2: Photodiode PCB block diagram. D1: photodiode (measurement device). C1: 1000 pF. R2: 510 Ω. IC1: Operational amplifier. Q1: JFET. Q2: +5 V regulator. Q3: −5 V regulator. Courtesy of Dr. Brynle Barrett, QSUM lab.

output of the photodiode while maintaining low voltage noise. A simplified circuit is presented in Fig. 4.3. R_F and C_F determine the frequency bandwidth through the equation $f_C = 1/2\pi C_F R_F$, and the output voltage is determined by $V_{OUT} = I_{PD} R_F$. The particular design used chooses the capacitance as $C_F = 1000\,\text{pF}$ and the resistances as $R_F = 510\,\Omega$. This selects a bandwidth $f_C \approx 300\,\text{kHz}$. In wavelength units, this detector only picks up signal in a 0.61 fm range about the desired frequency, greatly reducing background noise. Two such measurement devices were constructed in the course of this project while the third was reused from a previous experiment. The photodiode generates a current proportional to the optical power P incident on its active area: $I_{PD} = \mathbb{R}P$, where $\mathbb{R}(\lambda)$ is the photodiode's wavelength-dependent responsivity. For the photodiodes used in this circuit (Hamamatsu model S1223-01), the responsivity at $\lambda = 780$ nm is $\mathbb{R} = 0.52$ A/W. Applying the V_{OUT} relation, this implies a voltage response of $\sim 0.25\,\text{V}\,\text{mW}^{-1}$.

The output voltage of these circuits corresponds to the power of the light inci-

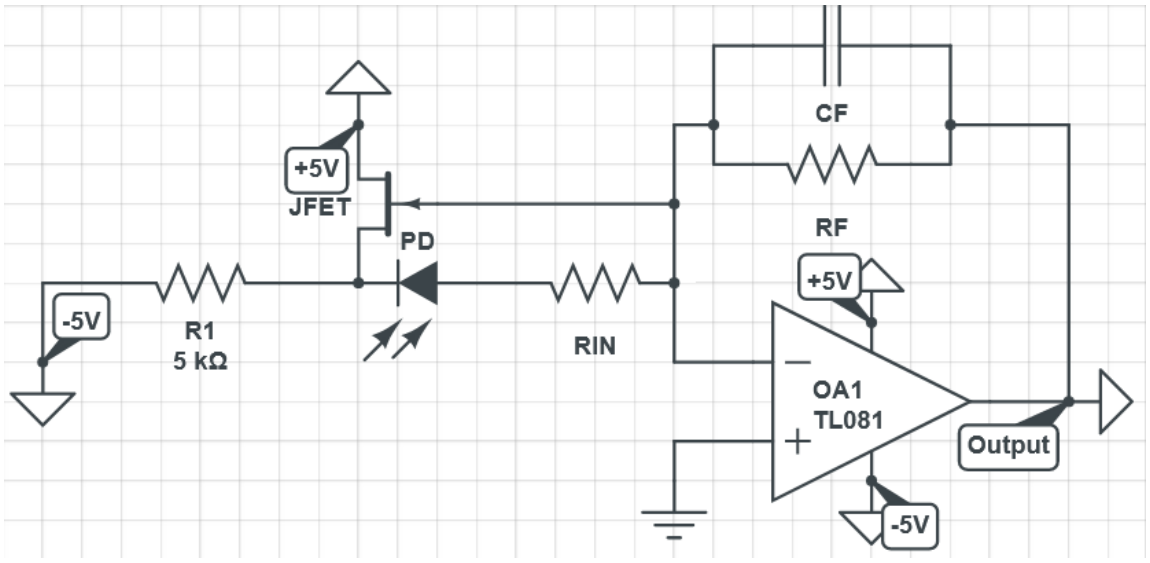

Figure 4.3: "Bootstrapping" implementation of a low-noise trans-impedance amplifier circuit.

Split #	P (mW)	V (V)	α (mW/V)
1st-order diff ted	4.05	0.844	4.80
1	2.35	0.676	3.48
2	2.50	0.648	3.86
3	2.86	0.674	4.24

Table 4.4: Example table of voltage from each photodiode compared to measured power to find conversion factors. (February 23, 2023).

dent on the photodiode by some linear relationship $P = \alpha(V + V_0)$. The sensitivity α was measured by comparing the output voltage of each detector with the power of its coupled light as measured by the Thorlabs power meter. α was calculated each time the system was turned on and stored in tables such as Table 4.4. Table 4.5 compares the conversion factors found on particular dates. Note that the conversion factors are consistent with the photodiode's stated response, $\frac{1}{\alpha} \sim \mathbb{R}R_F \approx \frac{V_{OUT}}{P}$, $\frac{1}{4.0} = 0.27\,\mathrm{V\,mW^{-1}}$. The offset voltage V_0 (assumed constant across all trials) was measured from the background data discussed below.

Examining Table 4.5, it is apparent that the photodiodes' average conversion ratios are very similar. Student's t-test ($t = \frac{\bar{X}_1 - \bar{X}_2}{s_p\sqrt{2/n}}$, where $\bar{X}_i$ is the sample mean of path i, n is the number of data points in each set, and s_p is the pooled standard

Date	Path 1	Path 2	Path 3	1^{st}-order diff$^{\underline{\text{ted}}}$
15/02/23	3.93	3.98	4.04	4.77
22/02/23	3.89	7.25	3.94	4.66
23/02/23	3.48	3.86	4.24	4.80
Average	3.8	5	4.0	4.74
S. D.	0.2	2	0.2	0.07

Table 4.5: Voltage conversion factors measured just following alignment.

deviation of the two sets $\sqrt{(s_1^2 + s_2^2)/2)}$ helps find the true difference between two uncertain values. Applying this test shows that the paths' conversion ratios are not very different at all. Paths 1 and 2 differ by $t = 0.18$, paths 2 and 3 by $t = 0.25$, and paths 1 and 3 by $t = 0.15$. Notably, the diodes were carefully realigned between the 22nd and the 23rd. This realignment process was prompted by the $\alpha = 7.25$ datapoint in path 2 on the 22^{nd}, which was taken as an outlier. This explains the difference in standard deviations between the different paths. It is not illuminating to compare the average or standard deviation in the fourth column to that in the other three as the 1^{st}-order diffracted beam was measured using a different device.

Each of the four measurement devices was connected to a four-channel data acquisition card (Measurement Computing model USB-231). The data acquisition card (DAC) boasts a 50 kS/s maximum sampling rate at 16 bits per sample. The DAC was in turn connected to the QSUM lab PC which used a script written by Kamal Shalaby to sample each channel at a predefined frequency over an extended period. There were two distinct tests conducted: a high-sample-rate (1 kHz) short-term test and a low-sample-rate 10 Hz long-term test. The short-term test provides more resolution in the time domain from which a larger frequency-domain power spectral density (PSD) can be derived, and the long-term test yields a lower resolution in time, but more information on the behaviour of the system on long timescales.

For each test, the data are plotted in three methods to aid analysis. The first is a simple time-series representation: the converted power is plotted against time. This allows a simple qualitative examination of the data. In particular, this plot

visualizes the decay of the coupling efficiency with time directly. Another use of the time-series representation is that it can show at a cursory glance any sudden changes in the laser power which do not follow the otherwise-established decay process.

The second analytical plot is a PSD. The integral $I = \int_{t_0}^{t_f} |x(t)|^2 \, dt$, where $x(t)$ is a signal measured at time t, can be rewritten using Parseval's theorem as $I = \int |\hat{x}(f)|^2 \, df$ where $\hat{x}(f)$ is the Fourier transform of the signal. The equation $\bar{S}_{xx}(f) = |\hat{x}(f)|^2$ is known as the power spectral density (PSD). This can be plotted to show the frequency-domain behaviour of the signal. It can be used as a measure of background noise levels and to identify frequency components in the signal.

The third plot generated with each dataset is the Allan deviation. The Allan deviation is commonly used as a measure of stability for different observation periods. It provides a direct measure of the standard deviation of the mean as a function of averaging time τ. For pure white Gaussian noise, the Allan deviation scales as $\sigma/\sqrt{\tau}$ (or a slope of $-\frac{1}{2}$ on a log-log scale). The Allan deviation gives a sensitive measure of drift in time series measurements in the form of curves that deviate from $1/\sqrt{\tau}$. For instance, $\sqrt{\tau}$ behaviour (slope $+\frac{1}{2}$) is a random walk. It follows from the Allan variance as calculated using sets of two samples over an observation period τ: $\sigma_A^2(\tau) = \frac{1}{2}\langle(\bar{y}_{n+1} - \bar{y}_n)^2\rangle$. The Allan deviation is $\sigma_A(t) = \sqrt{\sigma_A^2(t)}$.

Correlations between datasets are examined by plotting each dataset parametrically against other time-synchronized datasets. The Pearson R coefficient is then calculated for each pair of datasets as $R_{xy} = \frac{\sum_{i=1}^{n} x_i y_i - n\bar{x}\bar{y}}{(n-1)s_x s_y}$ where the s_q are the sample standard deviations. Examining the data in this way reveals the relationships between path couplings, and may help explain changes in coupling strengths.

When taking the correlation between the various photodiodes and the power meter data, a moving average of the power meter data was used instead of the raw data. A moving average replaces a data point with the average of the n points surrounding it. This smooths the output of the power meter, which is necessary when

Measurement Device	Average Offset (mV)	St. Dev. (mV)
Power Meter	1	2
Photodiode 1	-3.3	0.3
Photodiode 2	0	0.3
Photodiode 3	-11.4	0.3

Table 4.6: Voltage offsets by measurement device.

correlating with the much lower-noise (as shown below) photodiodes. If the moving average were not taken, the higher random noise of the power meter would mask the signal when compared to the data from the photodiodes. Without the moving average, correlations between the power meter and photodiode data are hidden by random noise. The exact value of n to be used is determined below.

Before beginning these tests, 5 min worth of data was collected at 1 kHz with the laser system powered off to ensure the measurement devices were stable on their own. These data were used to measure the offset voltage V_0 and any background noise due to electronics or room lights. From the PSD in Fig. 4.4, it is evident the three photodiodes (labeled Paths 1, 2, 3) are stable to $\sim 10^{-5}$ V, and the power meter (labeled AOM) is stable to $\sim 10^{-4}$ V after 1 s. The stabilities decrease over longer periods, as seen in the Allan deviation, but this is likely due to quantization noise in the DAC. Note that this decrease in stability is not present in the noisier AOM signal which is affected less by quantization noise. The offset voltage V_0 is found by taking the average value across the 5-minute time-series. These are listed in Tab. 4.6. Note that the standard deviations in the voltage offsets correspond to the first point on the Allan deviation curves, as expected for $\sigma_A(\tau)$ as $\tau \to 0$. Notably, the three photodiodes have different voltage offsets. This is likely because they were constructed by hand, so differences in the construction may introduce different offsets. All offsets are close to zero, so any differences in construction will not greatly affect the measurements.

From this data, it is possible to determine the value of n to be used in deter-

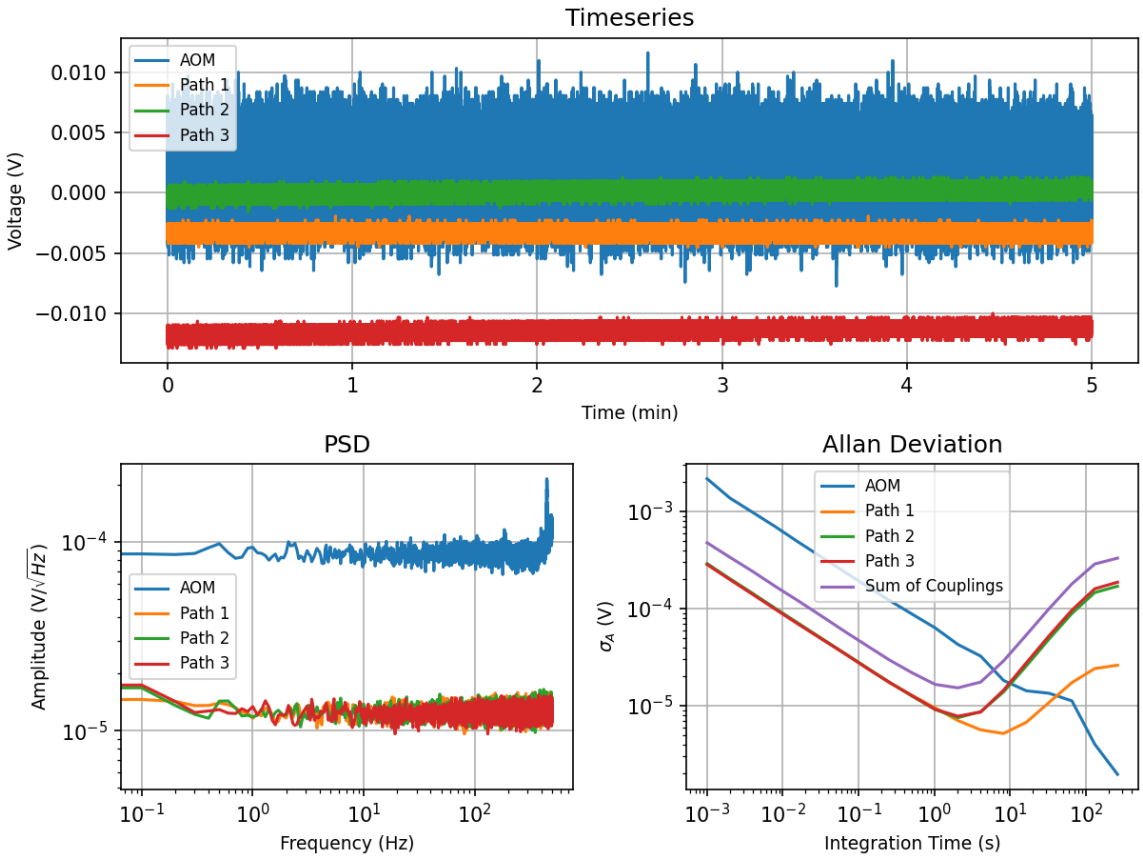

Figure 4.4: Data collected to find offsets in measurement devices' voltage output.

mining the moving average of the power meter. The value of n should be of the same order as the ratio of the random noise between the two instruments. If it's taken much higher than this, the noise in the other instrument will become dominant and the correlation will be hidden as before. In this case, taking the noise from the plateau of the PSD, $n \sim \frac{10^{-4}}{10^{-5}} \sim 10$ was chosen.

4.3.2.1 Short-Term Test

The system was first tested at a high sampling rate for a short period of time to find any quickly-varying effects on the laser power. For this test, the DAC was set to sample each channel at a rate of 1 kHz for a length of 1 h. Recording began shortly after the laser was powered on (about 15 min, as soon as the realignment process was complete). Collected data is plotted in Fig. 4.5.

Examining this dataset first qualitatively, it is apparent that there is a gradual decrease in the power of the system over the course of an hour. This is reflected not only in the 3 splitter paths but in the 1st-order diffraction from the AOM. Thus, this reduction must come from some portion of the optical pathway before the optical splitter section, possibly from the waveguide (which must be maintained at a fixed temperature to guarantee high conversion efficiency from 1560 nm to 780 nm) or the optical amplifier. Both have warm-up periods of 30-60 mins. so this is not surprising.

Examining the PSD section of the figure now, there are two regions of note. The tails to the right of the diagram are a measure of the background noise in each of the three detectors. Notably, there appears to be much less noise in the photodiodes (Paths 1-3) than in the power meter (AOM) — by about an order of magnitude. Also, all the splitting paths show groupings of peaks near 50-60 Hz.

Analyzing the PSD and the observed difference in noise, there are two possible explanations: either the power meter instrument is noisier than the photodiodes, or there is noise introduced by diffraction in the AOM. According to previous studies

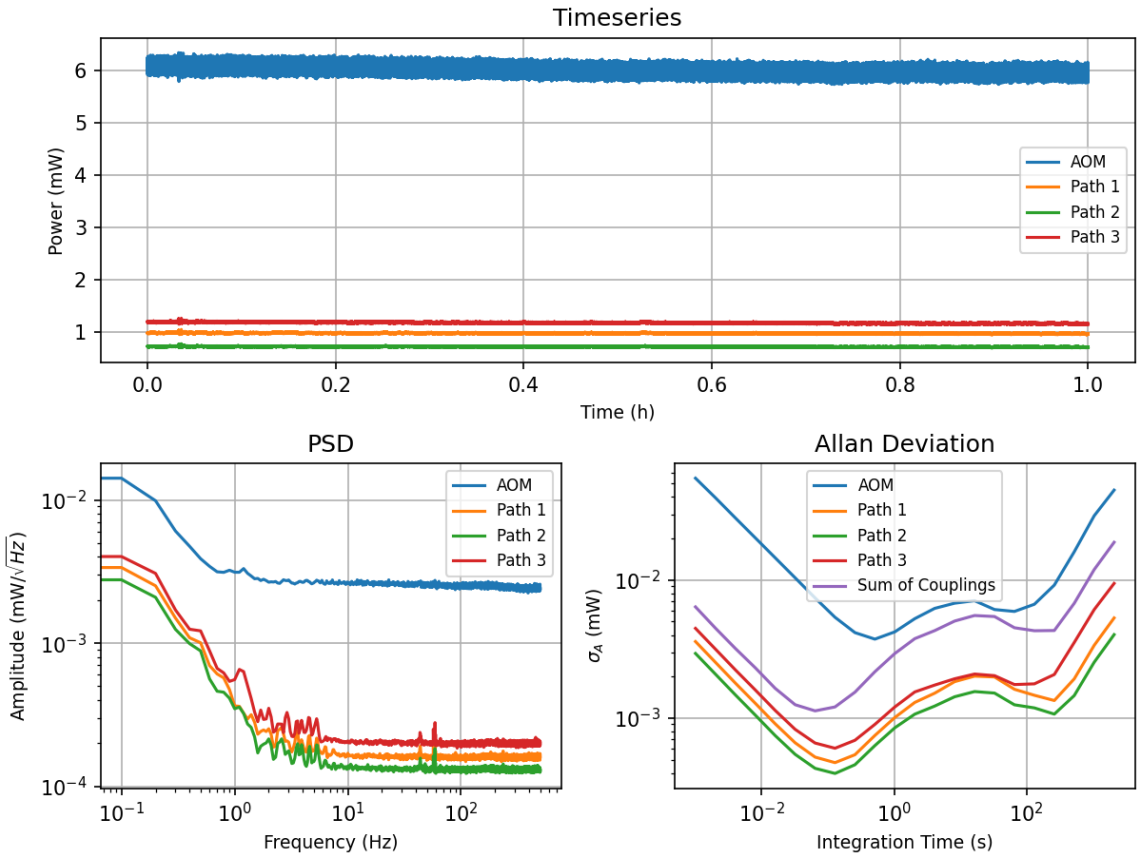

Figure 4.5: Data collected during short-term stability test of the various paths' fiber-optic couplings. Signals are converted to optical power in mV using Tab. 4.5 (data taken on 15/02/23).

on AOMs by other labs, the amplitude noise introduced by modulating input light is negligible (see [27]), suggesting the instrument may be to blame. With this in mind, alongside the relatively high noise in the power meter found even when the AOM was off in the background test, the power meter itself is likely the culprit.

The 50-60 Hz peaks are perplexing. Peaks of this frequency could correspond to interference from the 60 Hz mains. However, it is interesting that they did not appear in the background data. If these peaks do arise from mains interference, then, it must be through variation in the laser's power rather than variation in the power to the photodiodes. This warrants further investigation in the future, although, notably, these frequency components are already very small in amplitude ($< 3 \times 10^{-4}$ mW/$\sqrt{\text{Hz}}$). This is well below the noise floor of the power meter, which explains why these noise peaks do not appear in the AOM data. Varying laser power could cause disruptions to future experiments that would need to be compensated for.

The other region of note is the left side of the PSD. The broad peak at low frequency corresponds to the slow variation of the system throughout the test. It is possible to estimate the stability from the PSD alone, but the Allan deviation provides a more direct measure.

The Allan deviation provides a specific measure of the stability of the paths over a certain period. Accordingly, throughout ~ 0.1 s, the power in Path 3 varies by about 4×10^{-4} mW. The deviation reaches a stable point at ~ 10 s of 2×10^{-3} mW (or about 0.2%) and appears to oscillate about this value for higher timescales (ignoring the effect of quantization noise).

With the paths discussed on their own, it is informative to examine the correlations between the various paths (Fig. 4.6). By plotting the data of each path against each other path, it is possible to visualize their relationships. The Pearson R coefficient of linear correlation is set above each graph. The Pearson R coefficients

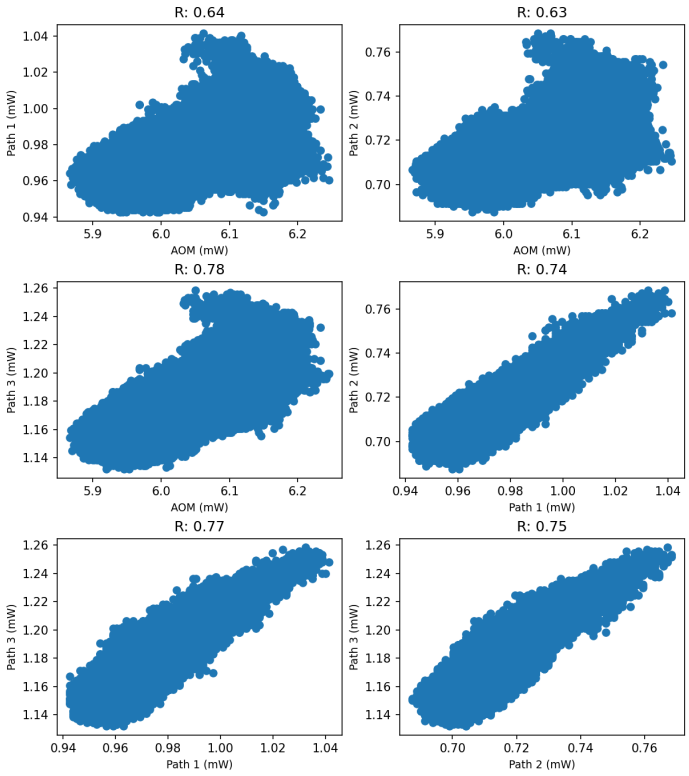

Figure 4.6: Correlation between various paths' power output during short-term stability test.

between each path (1-3 + AOM) are in the 0.6-0.8 range, which indicates a possible linear relationship.

The correlations of Fig. 4.6 indicate that changes in any one path are reflected in the other two paths. Given the similar correlation between the total power output (measured at the AOM), the output of the laser system itself may have varied throughout the test and caused a correlation between the paths.

Of note is the fact that the paths' correlations are strongly positive. This suggests that none of the paths are "stealing" light from the others through polarization drift, or that this stealing effect is small compared to other drift factors. If the initial polarization changed throughout the testing period, this would change the effect of the beam-splitting cubes and move some light from one path to the others, indicated by a negative correlation. This does not appear to be present (although further testing with the specific goal of measuring polarization drift is recommended).

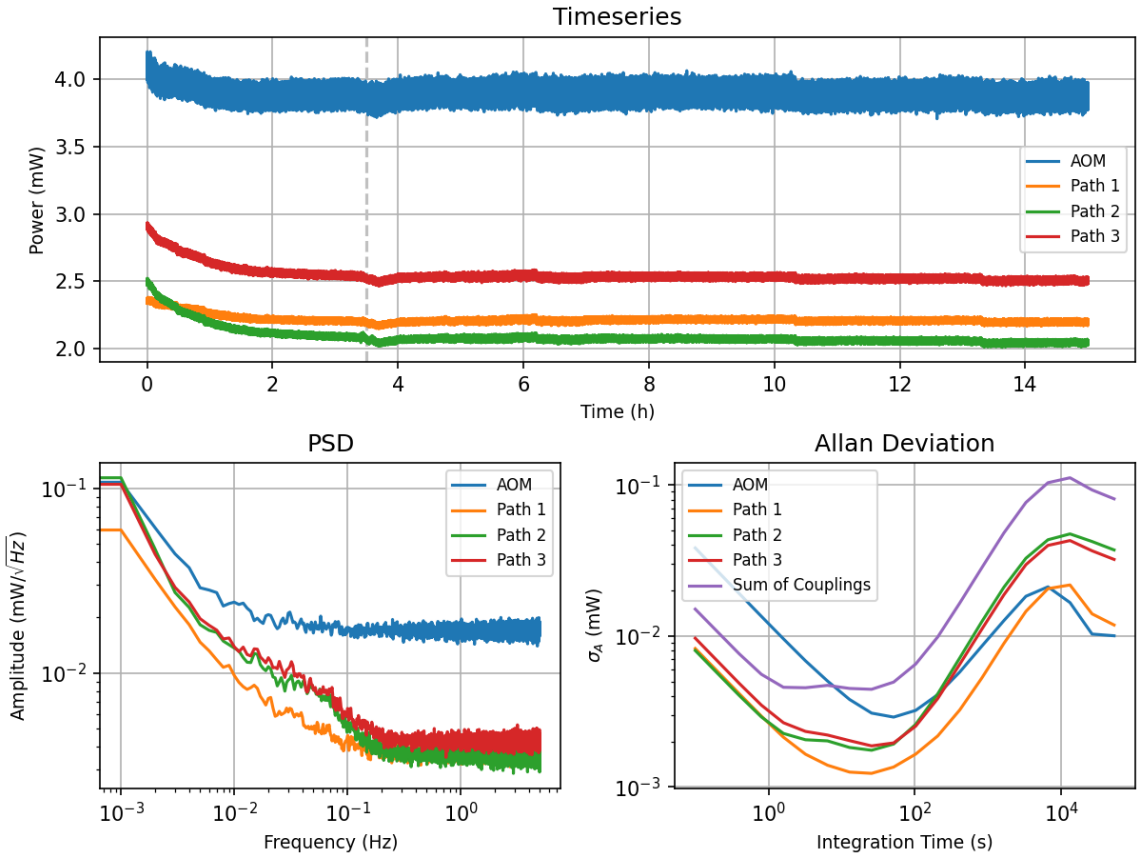

Figure 4.7: Data collected during the long-term stability test of the various paths' fiber-optic couplings. The dashed line indicates when researchers entered the lab.

4.3.2.2 Long-term test

The second test was performed overnight to determine the behaviour of the system in the long term. For this test, the sampling rate was reduced to 10 Hz, but the time was extended to 15 h. Before recording began, the optics were adjusted to optimize the fiber-coupling. Recording began shortly after the laser was powered on (about 15 min, as soon as the realignment process was complete). During the majority of the test, the lab was void of human activity and closed for the night. About 3 and a half hours after the beginning of the test, researchers entered the lab to check that the experiment was running properly. Collected data is plotted in Fig. 4.7.

The time series shows a sharp decay in the power of all the paths followed by a long period of moderate stability. Interestingly, there also exists a slow dip, lasting

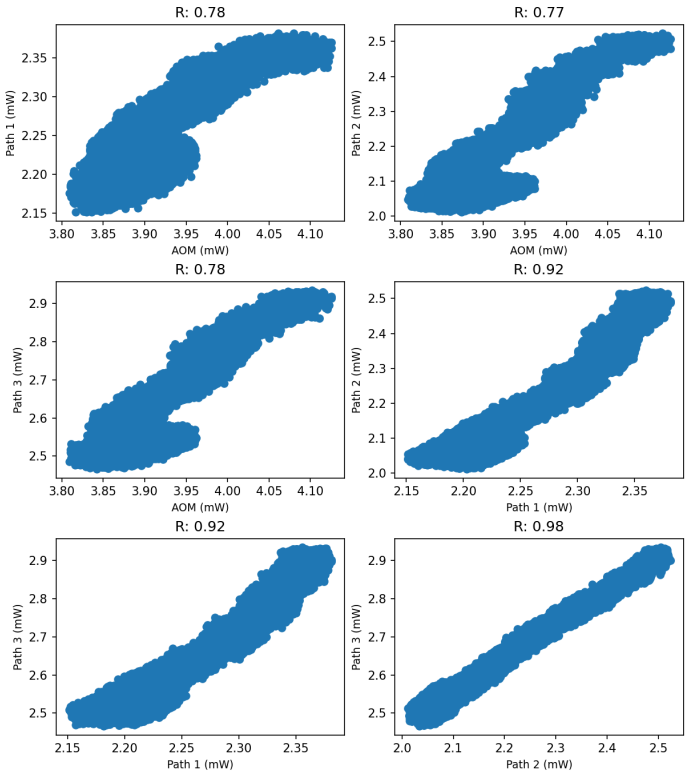

Figure 4.8: Correlation between various paths' power output during the long-term test.

30 min around the time that researchers re-entered the lab to check the status of the experiment. Paths 2 and 3 appear to decay more sharply in the first 2 hours than path 1 and the 1st-order diffraction from the AOM. During the period of relative stability, there are sharp drops in coupling efficiency of $\sim 4\%$. When these occur, they appear to be present in all four datasets at once.

The PSD displays a slowly-varying component related to the decay on the left, and decays to the background on the right. The PSD also shows a similar cluster as Fig. 4.5, where the noise profiles of the photodiodes are lower than that of the AOM. Notably, paths 2 and 3 have closer PSD curves than path 1.

The Allan deviation indicates the fiber splitting paths are stable up to about 20 s where the power reaches stability of 2×10^{-3} mW (or 0.1%). After this point, all paths show drift up to $\tau = 10^4$ s (~ 3 h) and settle around 4×10^{-2} mW (or 2%).

Measurements of correlation in these data are shown in Fig. 4.7. These show a

strong correlation between all three beam-split paths and a mid-strength relationship between the various paths and the 1st-order diffraction. The correlation between paths 2 and 3 is markedly higher than the correlation between paths 1 and 2 or paths 1 and 3. This high relative correlation indicates that one or both of these paths' shared optics (the $\lambda/2$-plate or the PBS cube) introduces some variation over time. As above, since the polarization is strongly positive, this is not likely polarization drift. It may be that the PBS or the $\lambda/2$-plate deforms slightly as the environment in the room changes, introducing some alignment drift.

Analyzing the time series of the long-term test data, it appears possible to split it into two distinct regions: a startup period (from $t = 0$ to 3.5 h) during which the couplings decay rapidly in an exponential-like curve and a stable period starting 4 h in during which the couplings decay more slowly but are subject to distinctive jumps. It is informative to examine these two regions separately.

A distinct feature of the 15 h dataset is the jumps in power in the stable period. These may arise from mode hopping in the optical amplifier. Mode hopping is a phenomenon whereby a laser "hops" between nearby frequency modes as environmental conditions in the room change (see [28]). Depending on the optics the laser passes through, this can generate jumps in intensity similar to those seen in the long-term test — for an example, see Fig. 4.9.

Mode-hopping may be reduced by several methods (see i.e [30], [31]). A system of wavelength-locking that may suppress mode-hopping in the QSUM lab was described in a previous honours thesis by Kamal Shalaby. This was not implemented during the long-term test, so its effectiveness in preventing intensity jumps due to mode-hopping is not discussed here.

Concerning data in the "startup region," (as shown in Fig. 4.10), the laser is relatively unstable. The power in each path changes significantly over the 3h period: in paths 2 and 3 the power drops by about 0.2 mW (or $\sim 8\%$). Although this drop

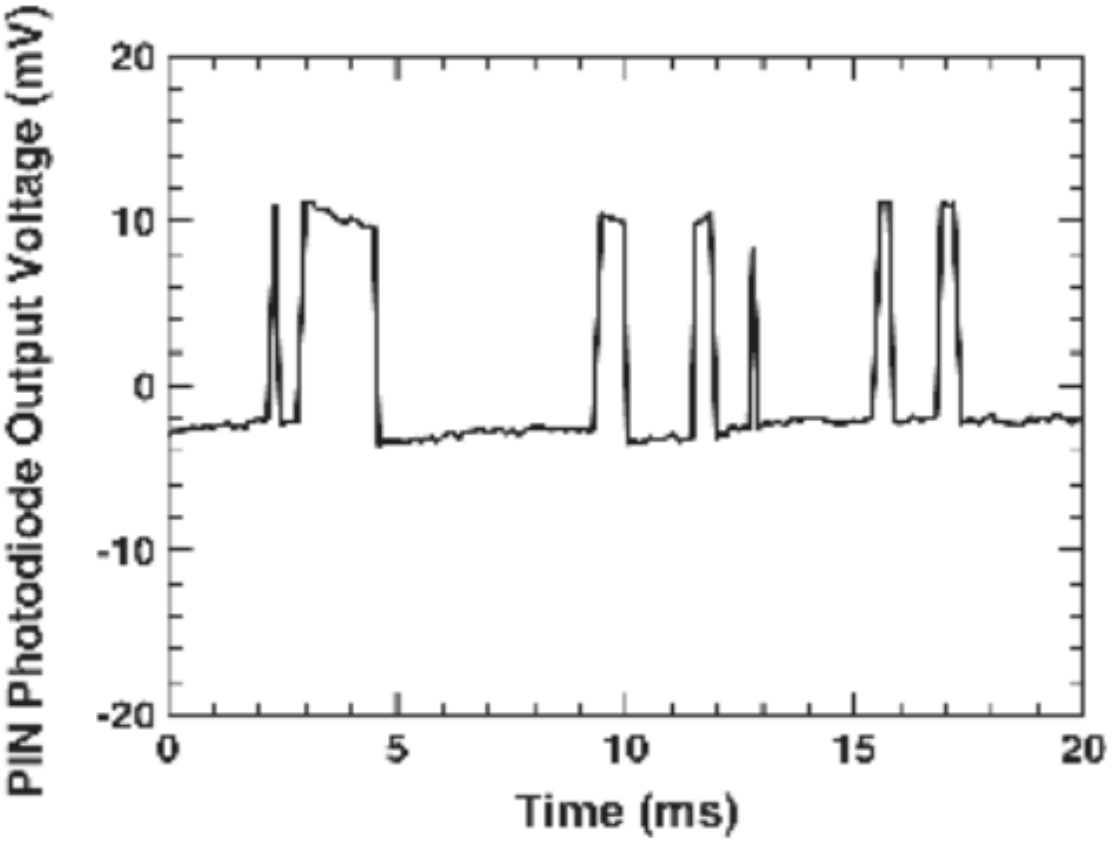

Figure 4.9: Effect of mode-hopping in a GaAs laser on the intensity of light measured by a photodiode. Mode-hopping changes the frequency output of the laser; this is measured in terms of intensity by reflecting the light from a piece of glass before being measured. At different wavelengths, different amounts of light are reflected/refracted affecting measured intensity. In this experiment, mode-hopping was induced by changing the current intentionally, so timescales are not comparable to timescales of the possible mode-hopping present in QSUM's study where the current input is intended to remain constant. Image taken from [29].

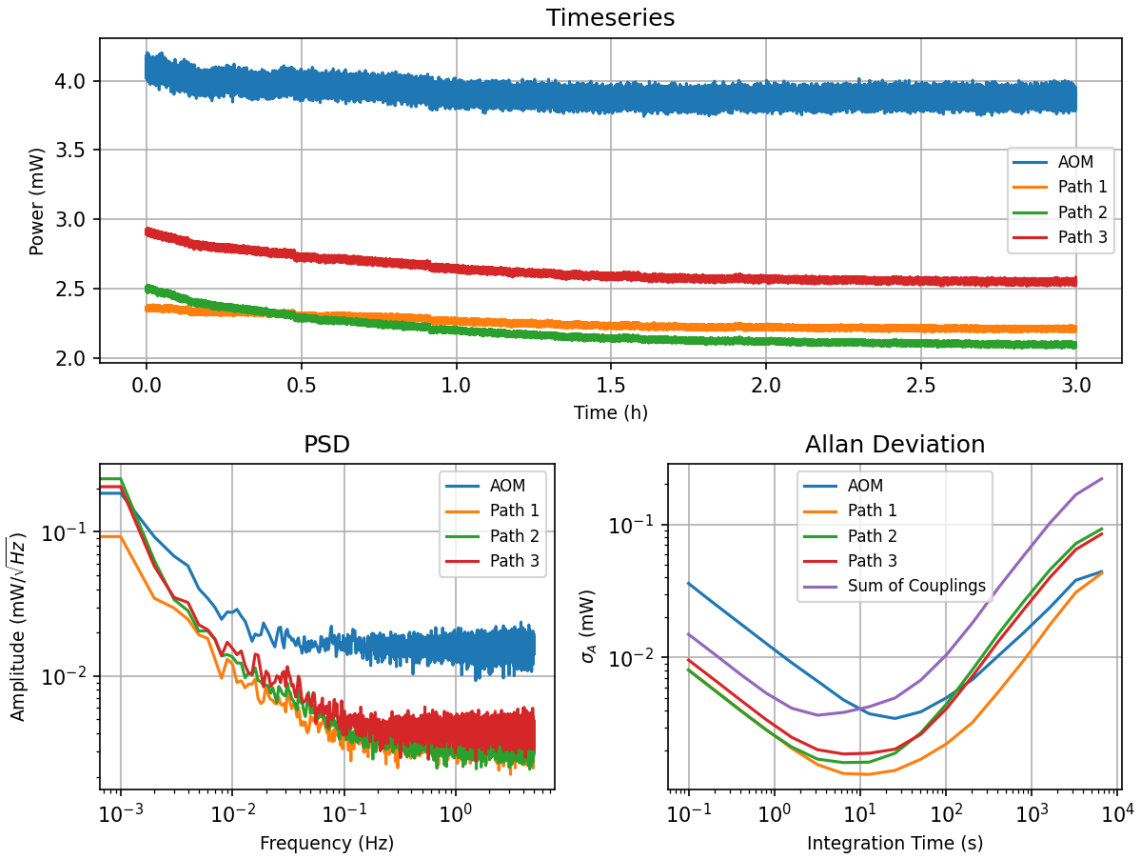

Figure 4.10: Data collected during the startup period of the long-term stability test.

is smaller in path 1, it is still present. The power changes similarly in the 1^{st}-order diffraction from the AOM.

The PSD shows a steep decay on the left side, indicating a high rate of change at low frequency (i.e. at long time scales). On the right side, the noise profile is similar to the 15 h case.

The Allan deviation reaches its lowest point around 10 s of integration time, where the paths reach about 2×10^{-3} mW of stability. This is similar to the full dataset, indicating that the startup period is responsible for most of the instability measured by the Allan deviation.

The correlations between the various paths are plotted in Fig. 4.11. They display the same trend in relationships between optical paths where 2 and 3 are very highly-correlated with $R = 0.99$, paths 1 and 2 and paths 1 and 3 are strongly correlated with $R = 0.97$. However, here, the correlation between the AOM and each path is similarly very high at around $R = 0.92$-0.95.

From these data, it is safe to say that the system is less stable during the first few hours after startup. Notably, although alignment drift in the three optical paths themselves is likely present, the strong correlation between the paths and the output of the AOM indicates the drift of total laser power is the dominant factor contributing to the change in power output.

Next, the stable period is plotted in Fig. 4.12. Once the system reaches a baseline, it appears to become very stable. The time series does not clearly show significant change across the period.

The PSD has a much more shallow drop between the left side and the right, indicating any drop in intensity is barely above the background noise as white noise appears as a flat, horizontal line in the PSD. Paths 2 and 3 again seem to share PSD curve features not present in path 1. Notably, all three photodiodes' PSDs show what appears to be a power law decay between their initial value and their

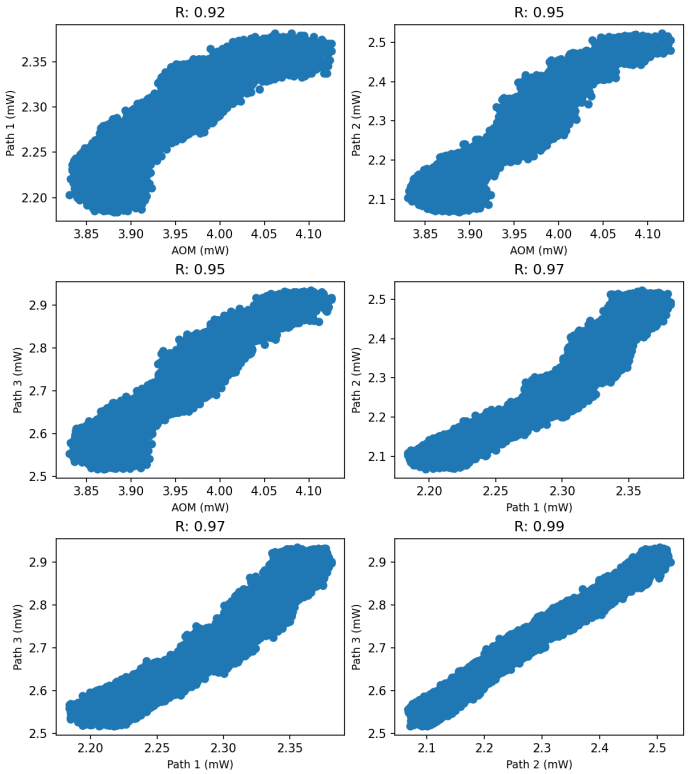

Figure 4.11: Correlation between various paths' power output during the startup period of the long-term test.

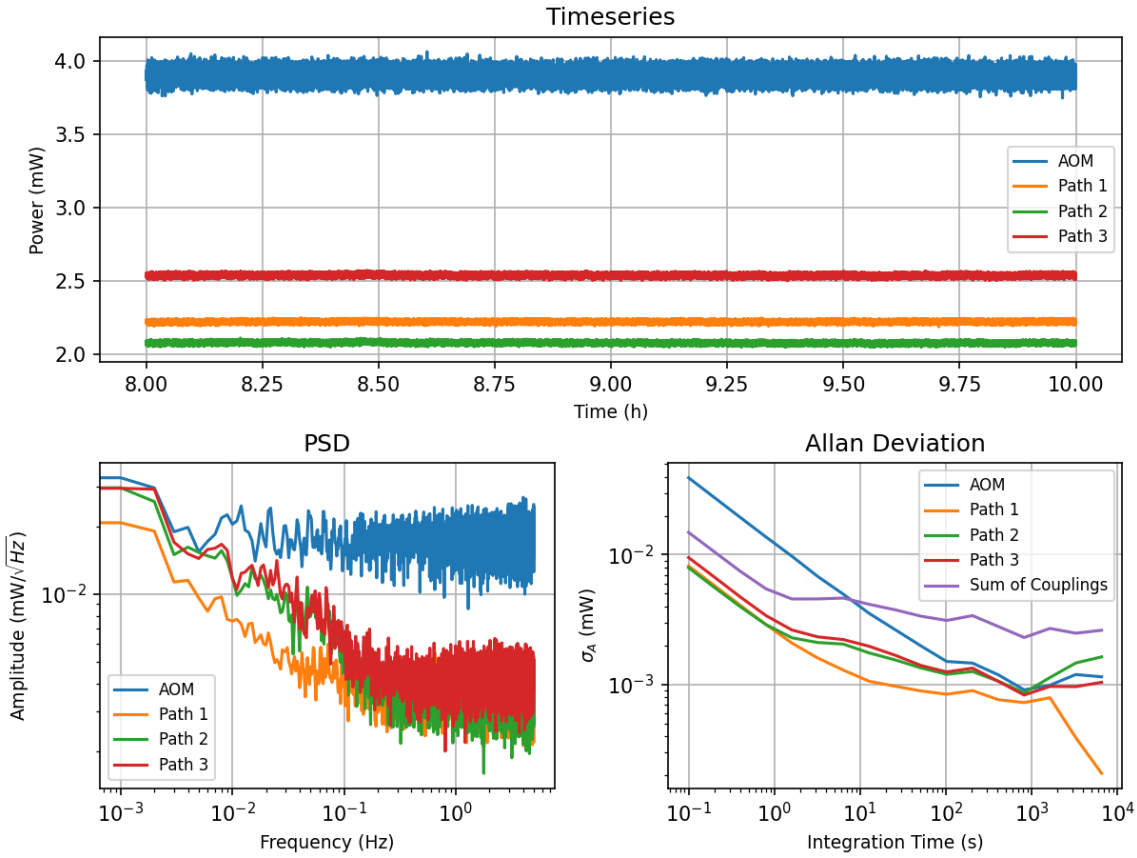

Figure 4.12: Data collected during a period of the long-term stability test during which coupling was particularly stable.

final, background level. This usually indicates decay caused by a natural source, and could come from air currents in the room modifying the alignment of the laser with time.

The Allan deviation shows the system maintains high stability, reaching below 10^{-3} mW (or 5×10^{-4} relative stability) even as the integration time approaches 2 h (9600 s).

The correlation of each path with each other is plotted in Fig. 4.13. Each path displays a low correlation with every other (although, notably, the correlation between paths 2 and 3 is still higher than any other). This indicates uncorrelated noise between the paths.

During periods between jumps in intensity, the optical paths in use are relatively

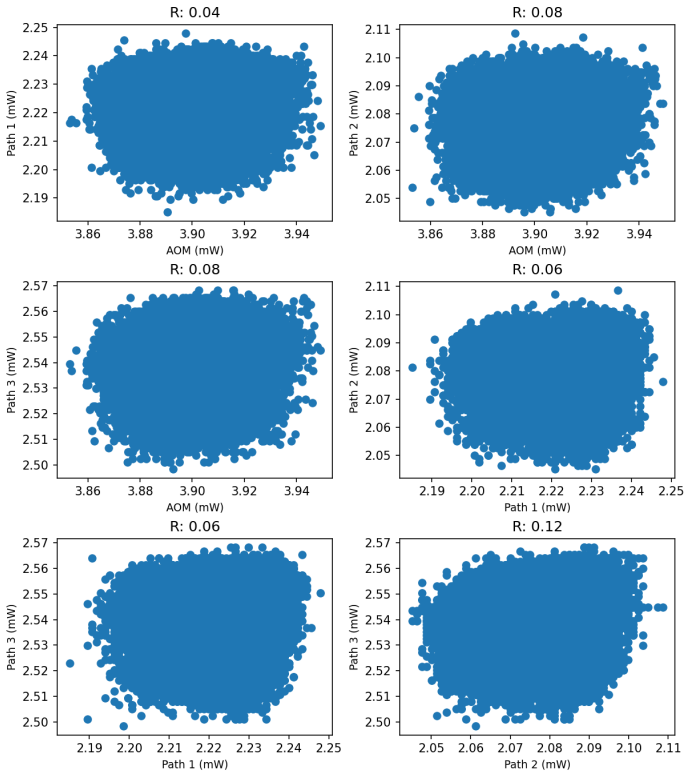

Figure 4.13: Correlation between various paths' power output during a particularly stable period of the long-term test.

stable. They change only in the µW range even over up to two hours. This is reflected in the low correlation between paths: the parameter being "correlated" between different paths is the random noise rather than any meaningful change in the system. Thus, a low correlation is expected.

Chapter 5

Conclusion and Future Work

5.1 Conclusion

This thesis consisted of three components related to the study of laser cooling in the QSUM lab. Chapter 2 discussed the theory of laser cooling, building from the theory of a two-level atom to the generation of an optical molasses surrounding a cloud of atoms. This chapter also discussed the process of magneto-optical trapping, whereby the velocity-dependent force from the optical cooling section is augmented by a position-dependent force.

In chapter 3, the equipment used in the QSUM lab was described. The equipment discussed ranged from the laser system itself to the optics used to split and focus the beam onto fiber-optics to the optics used to generate the desired beam profile for trapping in the $2D^+$-MOT.

Chapter 4 discussed the results of studies on the efficiency of an AOM, the speed of an optical shutter, and the stability of a set of optical couplings. The chapter began by characterizing the AOM, finding it to have an 80% transfer efficiency from the 0^{th}-order beam to the first-order diffraction. This was followed by a characterization of an optical shutter, which was found to take $\sim 1\,\text{ms}$ with a trigger-to-fall/rise delay

of $\sim 5\,\text{ms}$. Next, stability was discussed in two parts. A short-term, high-frequency test and a long-term, low-frequency test are presented and analyzed. The system is characterized as having a startup period during which it is less stable followed by long periods of high stability. During both the startup period and the stable period, jumps in intensity possibly caused by mode switching are present. Overall, during a stable 2 h period, the system was found to have relative stability of around 5×10^{-4}. Over 15 h, this relative stability decreased to about 2×10^{-2}.

5.2 Future Work

It remains to align the polarization of the fiber-coupled optical system discussed above. The polarization alignment is important to the trapping force in the $2D^+$-MOT. This will involve careful adjustments of the $\lambda/2$-plates coupling the three beams to their associated fiber-optics and measurement of polarization drift using a polarimeter. Analysis of polarization drift will follow a similar course as the analysis of coupling stability in the previous chapter. This will be conducted in early Summer 2023.

Once the polarization is properly aligned and stabilized, the first cold atoms can be achieved in the $2D^+$-MOT. This brings a whole host of new properties to characterize and optimize, from the trapping region to the flux of cold atoms through the pinhole.

Beyond the $2D^+$-MOT, another optical system very similar to the one described in this project will need to be established for the 3D-MOT. This will require the same level of characterization and analysis performed here.

Bibliography

[1] W. D. Phillips. Nobel lecture. https://www.nobelprize.org/prizes/physics/1997/phillips/lecture/.

[2] W. Ketterle. Nobel lecture. https://www.nobelprize.org/uploads/2018/06/ketterle-lecture.pdf.

[3] D. J. Wineland, R. E. Drullinger, and F. L. Walls. Radiation-pressure cooling of bound resonant absorbers. *Phys. Rev. Lett.*, 40:1639–1642, Jun 1978.

[4] H. J. Metcalf and P. van der Straten. *Laser cooling and trapping*. Springer-Verlag, New York, 1999.

[5] P. L. Chapovsky. Compact magneto-optical trap for rubidium atoms. *Journal of Experimental & Theoretical Physics*, 100(5):911 – 919, 2005.

[6] Q. Wang, Z. Wang, Z. Fu, W. Liu, and Q. Lin. A compact laser system for the cold atom gravimeter. *Optics Communications*, 358:82–87, 2016.

[7] M. H. Anderson, J. R. Ensher, M. R. Matthews, C. E. Wieman, and E. A. Cornell. Observation of bose-einstein condensation in a dilute atomic vapor. *Science*, 269(5221):198–201, 1995.

[8] U. Volz and H. Schmoranzer. Precision lifetime measurements on alkali atoms and on helium by beam- gas-laser spectroscopy. *Physica Scripta*, T65(48), 1996.

[9] D. Steck. Rubidium 87 D line data. Available online at: http://steck.us/alkalidata.

[10] E. L. Raab, M. Prentiss, A. Cable, S. Chu, and D. E. Pritchard. Trapping of neutral sodium atoms with radiation pressure. *Phys. Rev. Lett.*, 59:2631–2634, Dec 1987.

[11] J. Szczepkowski, E. Paul-Kwiek, G. Aub ock, L. Holler, C. Binder, and L. Windholz. Semiclasical model of magneto-optical trap depth. *Eur. Phys. J. Spec. Top.*, 144:265 – 271, 2007.

[12] W. D. Phillips and H. Metcalf. Laser deceleration of an atomic beam. *Phys. Rev. Lett.*, 48:596–599, Mar 1982.

[13] Z. T. Lu, K. L. Corwin, M. J. Renn, M. H. Anderson, E. A. Cornell, and C. E. Wieman. Low-velocity intense source of atoms from a magneto-optical trap. *Phys. Rev. Lett.*, 77:3331–3334, Oct 1996.

[14] B. Ghaffari, J. M. Gerton, W. I. McAlexander, K. E. Strecker, D. M. Homan, and R. G. Hulet. Laser-free slow atom source. *Phys. Rev. A*, 60:3878–3881, Nov 1999.

[15] J. Kellogg, D. Schlippert, J. Kohel, R. Thompson, D. Aveline, and N. Yu. A compact high-efficiency cold atom beam source. *Applied Physics B*, 109:61–64, 07 2011.

[16] S. Zhang, J. F. Chen, C. Liu, S. Zhou, M. M. T. Loy, G. K. L. Wong, and S. Du. A dark-line two-dimensional magneto-optical trap of ^{85}Rb atoms with high optical depth. *Review of Scientific Instruments*, 83(7):073102, 2012.

[17] D. Kim. QSUM lab summer 2021 work report. Unpublished report, 09 2021.

[18] S. Moir. QSUM lab summer 2022 report. Unpublished report, 09 2022.

[19] J. Schoser, A. Batär, R. Löw, V. Schweikhard, A. Grabowski, Yu. B. Ovchinnikov, and T. Pfau. Intense source of cold Rb atoms from a pure two-dimensional magneto-optical trap. *Phys. Rev. A*, 66:023410, 08 2002.

[20] Edmund Optics. Anamorphic prism pairs. https://www.edmundoptics.eu/knowledge-center/application-notes/optics/anamorphic-prism-pairs/. Accessed: 2023-03-01.

[21] P. Doherty. Galileoscope. http://www.exo.net/~pauld/workshops/Galileoscope.html. Accessed: 2023-03-01.

[22] Edmund Optics. What are beamsplitters? https://www.edmundoptics.eu/knowledge-center/application-notes/optics/what-are-beamsplitters/. Accessed: 2023-03-12.

[23] Edmund Optics. Understanding waveplates and retarders. https://www.edmundoptics.eu/knowledge-center/application-notes/optics/understanding-waveplates/. Accessed: 2023-03-12.

[24] BeamQLaser. AOM acousto optic modulator. https://beamq.com/laser/aom-acousto-optic-modulator-news/. Accessed: 2023-03-13.

[25] OFS Engineering and Marketing Staff. Fiber optics: Understanding the basics. https://www.photonics.com/Articles/Fiber_Optics_Understanding_the_Basics/a25151. Accessed: 2023-03-14.

[26] Schäfter + Kirchhoff. Collimated beam diameter of a singlemode fiber. https://www.sukhamburg.com/support/technotes/fiberoptics/coupling/collimatingsm/diameter.html. Accessed: 2023-04-03.

[27] F. Liu, L. Gu, S. Xie, X. He, D. Yi, M. Zhang, and Q. Tao. Acousto-optic modulation induced noises on heterodyne-interrogated interferometric fiber-optic sensors. *Journal of Lightwave Technology*, 36(16):3465–3471, 2018.

[28] T. A. Heumier. *Mode Hopping in Semiconductor Lasers*. PhD thesis, Montana State University, MT, 1992.

[29] T. A. Heumier and J. L. Carlsten. Mode hopping in semiconductor lasers. Technical report, ILX Lightwave, 1995.

[30] Y. Liu, J. Zhang, Z. Jia, D. Yao, F. Yan, F. Liu, L. Wang, J. Liu, and Z. Wang. Stable single mode operation of quantum cascade lasers by complex-coupled second-order distributed feedback grating. *Solid-State Electronics*, 103:79–82, 2015.

[31] A. Mahmoud and M. Ahmed. Effect of asymmetric intermodal gain suppression on dynamics of multimode semiconductor lasers. *Optics Communications*, 462:125365, 2020.